JAMES | Journal of Advances in Modeling Earth Systems

RESEARCH ARTICLE
10.1029/2022MS003556

On Dynamical Decomposition of Multiscale Oceanic Motions

Chuanyin Wang[1], Zhiyu Liu[1], and Hongyang Lin[1]

[1]State Key Laboratory of Marine Environmental Science, Department of Physical Oceanography, College of Ocean and Earth Sciences, Xiamen University, Xiamen, China

Key Points:

- Dynamics-based decomposition methodologies are developed for diagnostic analysis of global, tide-resolving, and submesoscale-admitting simulations
- Compared with decompositions based on (assumed) scale separations, extracting low-mode internal gravity waves (IGWs) via dispersion relations respects the underlying dynamics
- The challenge of separating high-mode IGWs and submesoscale flows is tackled by a dynamics-based spectral decomposition that can naturally handle aliasing of IGWs

Supporting Information:

Supporting Information may be found in the online version of this article.

Correspondence to:

Z. Liu,
zyliu@xmu.edu.cn

Citation:

Wang, C., Liu, Z., & Lin, H. (2023). On dynamical decomposition of multiscale oceanic motions. *Journal of Advances in Modeling Earth Systems*, *15*, e2022MS003556. https://doi.org/10.1029/2022MS003556

Received 29 NOV 2022
Accepted 4 MAR 2023

Abstract The ocean hosts a variety of fluid motions characterized by contrasting dynamical regimes and spatiotemporal scales. A practical decomposition of multiscale motions in realistic oceanic settings is crucial to advancing dynamical interpretation and prediction of oceanic processes, but remains a major challenge. To this end, methodology is developed in this study for decomposing multiscale oceanic motions based on their respective dynamical characteristics. Specifically, large-scale currents and barotropic tides have the largest horizontal scales but contrasting frequencies; low-mode internal gravity waves (IGWs) are well constrained by linear dispersion relations, whereas mesoscale flows are of relatively low frequency and with horizontal scales above the first baroclinic deformation radius; the *intrinsic* frequency of high-mode IGWs (submesoscale flows) is above (well below) the inertial frequency. The validity and usefulness of the proposed methodology are demonstrated with a proof-of-concept application to simulated flows in the central basin of the South China Sea.

Plain Language Summary There are multiple types of oceanic motions, which can generally be divided into large-scale circulations, (sub)mesoscale currents, barotropic tides and internal gravity waves (IGWs). These motions have contrasting physical characteristics and thus differing time and space scales. Separating one motion from another is a natural need to gain a better understanding of each type of motion. In this study, we develop methodology for separating the full flow into different components utilizing physical constraints of each type of motion. In particular, low-mode IGWs (i.e., IGWs with relatively large wavelength) are isolated according to their dispersion relation (i.e., a quantitative relationship between their time and space scales), while high-mode IGWs (i.e., IGWs with relatively short wavelength) are separated from submesoscale currents based on the relative spectral magnitude of relative vorticity and horizontal divergence. We show, with a proof-of-concept application to numerically simulated flows in the South China Sea, that the proposed methodology is valid and efficient.

1. Introduction

It is well established that oceanic horizontal kinetic energy spectra in log-log coordinates feature a large-scale plateau at low frequencies, a falling constant-slope band due to mesoscale variability and an internal gravity wave continuum interleaved with peaks at near-inertial and tidal frequencies (Ferrari & Wunsch, 2009; Fu et al., 1982). These spectral characteristics have been confirmed by numerous observations, including the McLane profiling data scattered around the Pacific (Savage, Arbic, Alford, et al., 2017), tidal gauge data (Savage, Arbic, Richman, et al., 2017), and moored measurements distributed globally (Luecke et al., 2020). Nevertheless, recent studies based on high-resolution observations and numerical simulations demonstrate that this view needs to be refined. For example, low-frequency submesoscale flows have overlaps in timescale with mesoscale flows but are characterized by wavenumber spectra with different slopes (Capet et al., 2008); similarly, high-frequency submesoscale flows have overlaps in timescale with internal gravity waves (IGWs) (Bühler et al., 2014; Torres et al., 2018), especially in strong currents such as the Kuroshio, the Gulf Stream, and the Antarctic Circumpolar Current (von Storch et al., 2019). In realistic oceanic settings, balanced flows (e.g., large-scale currents, mesoscale and submesoscale flows) and unbalanced flows (e.g., barotropic tides and IGWs) coexist and interact, to different extents, with one another. This naturally raises the need for flow decomposition to reveal the respective characteristics of multiscale oceanic motions and examine their dynamical interactions. Normally, filtering-based or flow-oriented approaches are used to decompose the simulated full flow of numerical models.

Eulerian filtering, including temporal filtering, spatial filtering, spatiotemporal filtering, is a filtering-based approach in the Eulerian frame of reference. In an idealized *f*-plane simulation of a baroclinically unstable channel flow, Barkan et al. (2017) associated temporally lowpass-, bandpass-, and highpass-filtered fields with mesoscales, submesoscales, and IGWs, respectively. Spatial filtering of the vertical velocity was used by Sugimoto and

Plougonven (2016) to separate smaller-scale IGWs emitted from an idealized larger-scale eddy dipole on an *f* plane. On the basis of a significant discontinuity in the slope of summertime sea surface height (SSH) wavenumber spectra, Torres et al. (2019) accomplished unbalanced-balanced flow decomposition through an equivalent spatial filtering in order to characterize unbalanced-balanced energy exchange. Spatiotemporal filtering has been recently proposed by Qiu et al. (2018) and Torres et al. (2018). Based on outputs from a global, tide-resolving and submesoscale-admitting simulation termed as LLC4320 (Rocha, Chereskin, et al., 2016; Rocha, Gille, et al., 2016), Qiu et al. (2018) computed frequency-wavenumber spectra of surface horizontal velocity and SSH, attributed the energies above the dispersion relation curve of mode-10 IGWs and tidal frequencies to unbalanced flows, attributed the energies below to balanced flows, defined the transition length scale from balanced to unbalanced flows and explored seasonality of this transition scale over the global ocean. Also using the LLC4320 simulation, Torres et al. (2018) extended similar partitioning analysis, but only relying on the dispersion relation of mode-10 IGWs, to other surface-ocean variables such as relative vorticity, horizontal divergence, and sea surface temperature. Although Eulerian filtering works well for specific settings or specific purposes, notable overlaps exist among the decomposed components (e.g., Jones et al., 2023, Preprint), raising concerns on their generic applicability to process studies focusing on interaction mechanisms which require the decomposition to be as accurate as possible.

As another kind of filtering-based approach, Lagrangian filtering is recently developed to isolate IGWs and has been applied to a number of idealized or realistic (e.g., spontaneous internal-wave-generating or internal-tide-resolving) configurations (Bachman et al., 2020; Nagai et al., 2015; Shakespeare & Hogg, 2017, 2019; Shakespeare et al., 2021). In contrast to Eulerian filtering, Lagrangian filtering, which is designed to address the Doppler shift issue, operationally identifies IGWs as flows with frequencies above the inertial frequency in a frame of reference moving with the *full* flow. Although it represents an ingenious effort in multiscale flow decomposition, Lagrangian filtering requires particle tracking and is thus computationally expensive.

Flow-oriented approaches exploit balanced dynamics (e.g., quasi-geostrophic (QG) theory) for flow decomposition. Balanced flows, especially mesoscale flows, by definition are essentially governed by the balanced dynamics (e.g., QG theory). It is thus feasible to separate balanced flows from IGWs by imposing underlying dynamical constraints. For example, Danioux et al. (2012) first diagnosed the QG vertical velocity and then took the difference between the total vertical velocity and the QG estimate as that due to IGWs which were generated spontaneously by a zonal flow undergoing baroclinic instability. A similar idea worked moderately well in isolating tidal SSH from an unstable baroclinic jet subject to idealized tidal forcing (A. L. Ponte et al., 2017). Obviously, efficiency of these methods is highly dependent on the applicability and accuracy of the assumed dynamical constraints (von Storch et al., 2019). In fact, the QG omega equation cannot account for all contributions from balanced motions (Danioux et al., 2012).

Here, we seek to develop dynamics-based methodologies that can be operationally used to decompose the full flow, as unambiguously as possible, into large-scale currents, barotropic tides, low-mode IGWs, mesoscale flows, high-mode IGWs, and submesoscale flows. Specifically, large-scale currents and barotropic tides are isolated as flows with the largest horizontal scale and are further separated from each other through temporal filtering; mode-1 and mode-2 IGWs, together termed as low-mode IGWs, are extracted according to their dispersion relations to guarantee that the polarization relations are satisfied in a dynamically consistent manner; mesoscale flows are recovered as the low-frequency flows with the horizontal scale larger than the first baroclinic deformation radius; high-mode IGWs (i.e., IGWs excluding low-mode IGWs) and submesoscale flows are distinguished from each other based on the relative size of spectral magnitudes of the horizontal divergence and relative vorticity, without any a priori assumption that submesoscale flows (high-mode IGWs) are non-divergent/weakly divergent (irrotational).

The paper is organized as follows. Section 2 introduces the LLC4320 simulation. Section 3 develops the methodology of decomposition. Section 4 evaluates the decomposition methodology in the South China Sea (SCS), particularly focusing on examination of the dynamical consistency among variables for each decomposed flow regime. This paper concludes with a discussion in Section 5 and a summary in Section 6.

2. The LLC4320 Simulation

The global 1/48° LLC4320 simulation is based on the Massachusetts Institute of Technology general circulation model (MITgcm; Marshall et al., 1997) and outputs hourly snapshots for 14 months, from September 2011 to

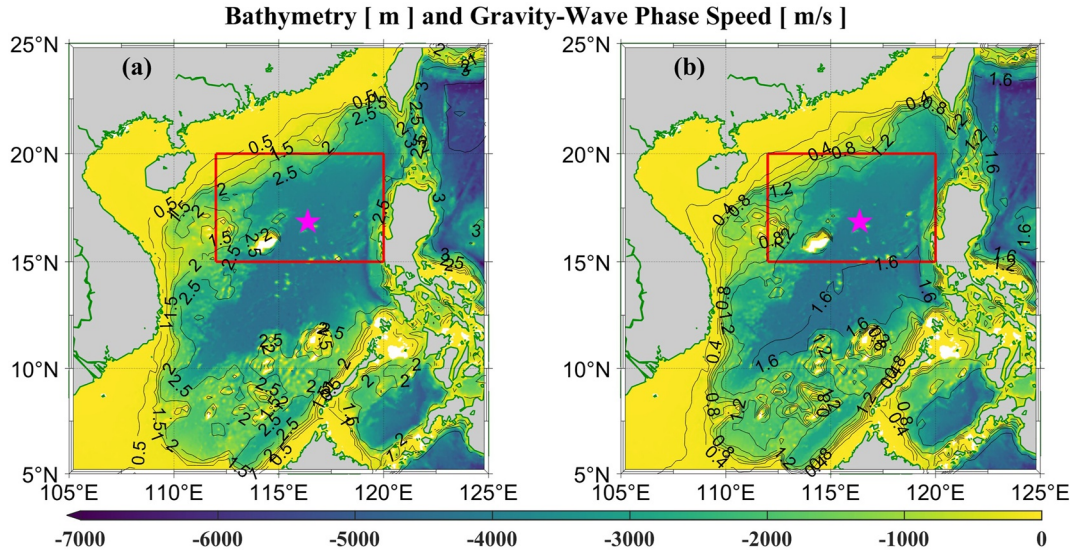

Figure 1. ETOPO1 bathymetry (shading) and the gravity-wave phase speeds (contours) of the South China Sea and adjacent regions. The gravity-wave phase speeds for the (a) first and (b) second baroclinic modes are calculated using a MATLAB script (i.e., dynmodes.m; https://sea-mat.github.io/sea-mat/) based on the World Ocean Atlas (WOA2018). The red rectangle indicates our study region and the magenta pentagram shows the location of the extracted mooring data discussed in Section 3.1.

November 2012. The vertical grid spacing varies from 1 m at the surface to ~30 m near the 500-m depth, with 40 vertical levels in the top 525 m. At the surface, the simulation is forced by 6-hourly atmospheric fields from the 0.14° European Center for Medium-Range Weather Forecasts atmospheric operational model analysis. Astronomical tidal forcing, in terms of the full luni-solar potential, is applied to the MITgcm as an additional atmospheric pressure forcing (R. Ponte et al., 2015). Readers are referred to Arbic et al. (2018) for a detailed description of the LLC4320 simulation configuration.

Several previous studies have evaluated various aspects of the LLC4320 simulation against observations (e.g., Luecke et al., 2020; Qiu et al., 2018; Rocha, Chereskin, et al., 2016; Rocha, Gille, et al., 2016; Savage, Arbic, Alford, et al., 2017; Savage, Arbic, Richman, et al., 2017; J. Wang et al., 2018; Yu et al., 2019). A complete summary is beyond the scope of this study but we note that the simulated large-scale currents (J. Wang et al., 2018), mesoscale variabilities (Qiu et al., 2018) and super-inertial flows (Savage, Arbic, Alford, et al., 2017) generally agree well with the observations.

The SCS is featured by well-developed basin-scale circulation (e.g., Hu et al., 2000), energetic barotropic tides (e.g., Zu et al., 2008), enormously strong internal tides (Zaron, 2019; Zhao, 2014), intense mesoscale activity (Cheng & Qi, 2010; Chen et al., 2011; Chu et al., 2020), and abundant submesoscale features (Lin et al., 2020; Ni et al., 2021). Lin et al. (2020) evaluated LLC4320 simulation outputs in the SCS against both moored and remote-sensing observations. They concluded that the basin-scale circulations, mesoscale and submesoscale variabilities, and tidal motions are reproduced with a high degree of realism. As such, the outputs of the LLC4320 simulation in the SCS can serve as a virtual laboratory for evaluating the proposed flow-decomposition methodology. Specifically, we select a sub-region of the central SCS indicated by the red rectangle in Figure 1 to carry out our analysis.

3. Methodology

The frequency-wavenumber spectra were the basis of several recent LLC4320-based studies (e.g., Qiu et al., 2018; Savage, Arbic, Alford, et al., 2017; Torres et al., 2018). The starting point for our decomposition is also frequency-wavenumber spectra. Here the decomposition is illustrated using SSH; other variables are decomposed following the same approach. The LLC4320 simulated SSH in the study region is collected in a three-dimensional (3D) matrix (zonal, meridional, and temporal), namely $\eta_{\mathrm{Full}}(x, y, t)$. Missing values due to bathymetry are interpolated/extrapolated by means of the discrete cosine transform (Garcia, 2010; G. Wang et al., 2012). Following

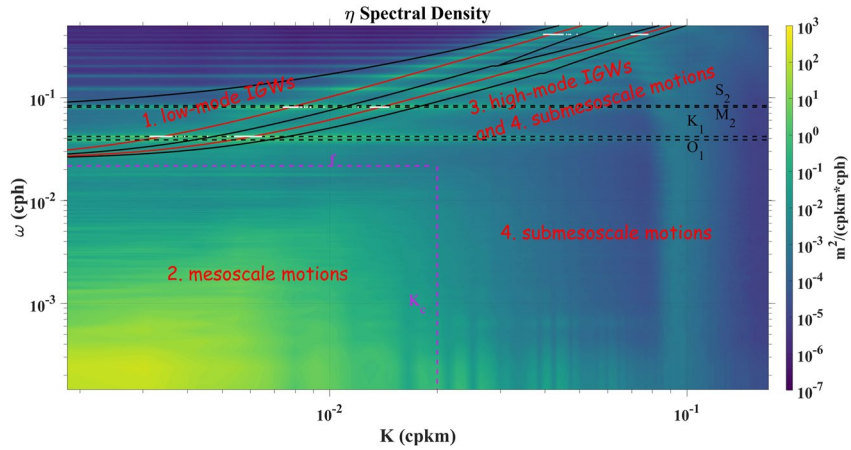

Figure 2. Frequency-wavenumber spectra of simulated sea surface height in the red-rectangle region of Figure 1. The red curves depict dispersion relations for mode-1 and mode-2 internal gravity waves (IGWs). The solid black curves surrounding them delimit what is defined as low-mode IGWs in this study. The dashed black lines indicate diurnal (K_1, O_1) and semidiurnal (M_2, S_2) tidal frequencies. The horizontal magenta line represents the cutoff frequency (i.e., the inertial frequency at the southern edge of the study region) between low-mode IGWs and mesoscale motions. The vertical magenta line marks the cutoff wavenumber (i.e., the wavenumber corresponding to the minima of the first baroclinic deformation radii in the study region) between mesoscale and submesoscale motions. The white dots on the K_1, M_2 and 0.4-cph lines indicate ray-traced wavenumbers detailed in Section 5.1. Also defined and labeled are (a) low-mode IGWs, (b) mesoscale motions, (c) high-mode IGWs, and (d) submesoscale motions.

standard practice, the mean and linear trend are removed in each dimension and the matrix is then multiplied by a 3D Tukey window with a taper-constant ratio of 0.2 (Arbic et al., 2014), producing the modified matrix $\eta_{m\text{Full}}$. By applying the Fourier transform to $\eta_{m\text{Full}}$ and taking the azimuthal average (Savage, Arbic, Alford, et al., 2017), the frequency-wavenumber spectra are finally obtained (Figure 2). For clarity, various oceanic motions that the spectra can resolve are labeled in Figure 2. These motions will be separated based on their respective dynamical characteristics. It is necessary to note that the mean and trend are not actually discarded and will be immediately shown to include important flow components.

3.1. Separating Large-Scale Currents and Barotropic Tides

Large-scale currents have a horizontal scale of $O(10^3)$ km and have frequencies much lower than the inertial frequency. Barotropic tides have a similar horizontal scale to large-scale currents but have super-inertial frequencies. Due to their large horizontal scale, both large-scale currents and barotropic tides are contained in the mean and linear trend mentioned above. Further separation of large-scale currents from barotropic tides can be accomplished via tidal harmonic analysis using for example T_TIDE (Pawlowicz et al., 2002) or simply via a 3-day lowpass-highpass filtering. As an example, Figure 3 shows SSH time series for the mean and linear trend at a randomly selected location (116.39°E, 16.85°N; denoted by the magenta pentagram in Figure 1). Evidently, barotropic tides (blue and green curves) account for a considerable proportion of the total variability, in agreement with dynamical characteristics of the study region (e.g., Yan et al., 2020; Zu et al., 2008). The large-scale currents (black curve), including geostrophic and Ekman components, show a significant seasonal variation essentially in response to the seasonally reversing monsoonal wind forcing (e.g., Hu et al., 2000).

3.2. Extracting Low-Mode IGWs

Low-mode IGWs are defined to be mode-1 and mode-2 IGWs which are extracted according to their dispersion relations. The low-mode IGWs are delimited in Figure 2. The unique dynamical feature of IGWs is that they are well-constrained by theoretical dispersion relations. As an example, the dispersion relation curves of mode-1 and mode-2 IGWs, which are calculated from the temporally averaged model density profile at a location right in the middle of the study region, are shown in Figure 2 as red curves. Remarkably, the super-inertial energy is mostly concentrated along the dispersion relation curves. We can thus extract IGWs using signals along those curves. Nonetheless, due to the influence of the background flow and spatial variation of the stratification, the energy of

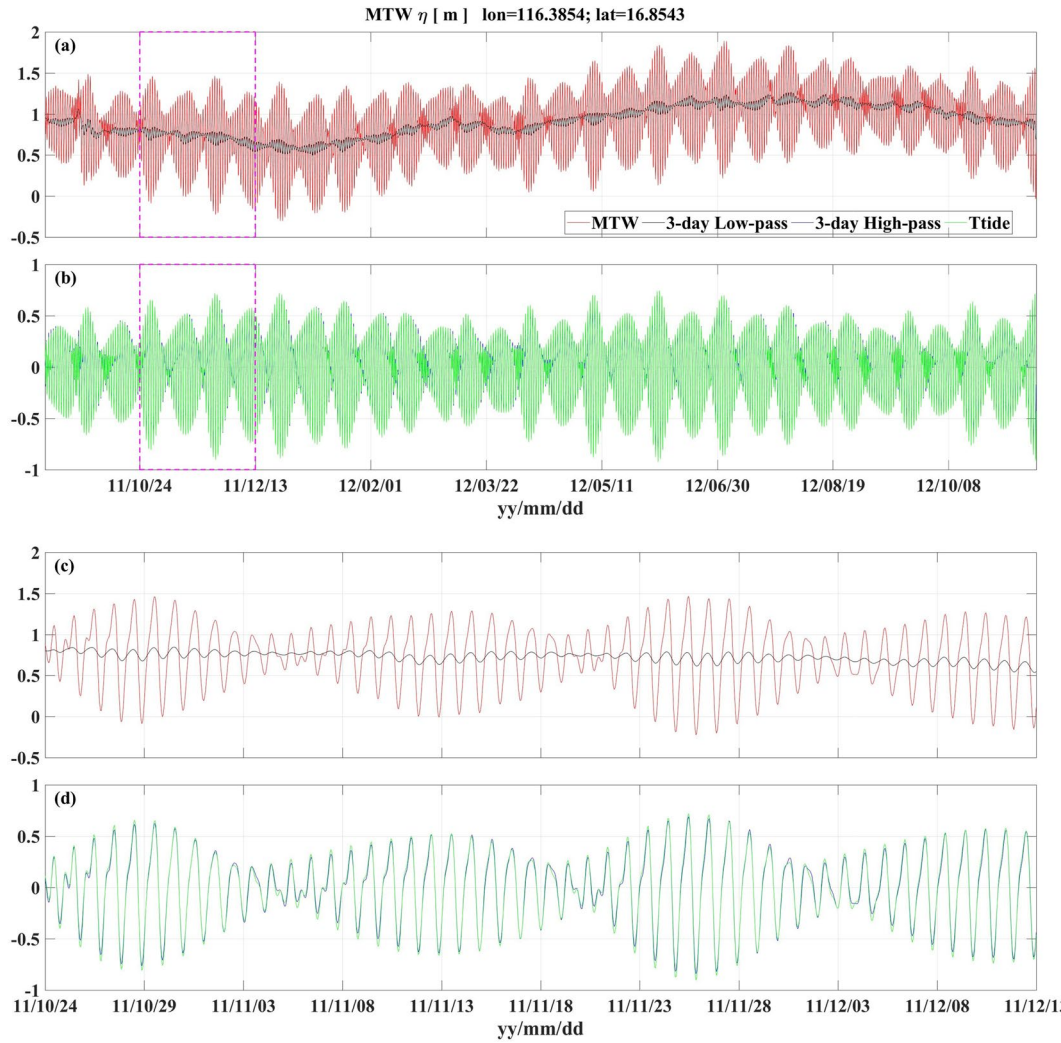

Figure 3. Sea surface height time series for the mean and linear trend at a randomly selected location (indicated by the magenta pentagram in Figure 1) in the study region. The red curve in panels (a, c) shows the time series of the removed mean and linear trend (MTW, i.e., Mean, Trend, Windowing). The black curve in panels (a, c) indicates the 3-day lowpass-filtered time series (i.e., large-scale currents). The blue curve in panels (b, d) denotes the 3-day highpass-filtered time series, and the green curve in panels (b, d) is obtained through tidal harmonic analysis (i.e., two different estimates of barotropic tides). Panels (c, d) are the same as (a, b), respectively, but zoomed in for the period highlighted in magenta in panels (a, b). Note the different *y*-axis ranges.

IGWs is not precisely concentrated along the red dispersion relation curves which are obtained based on a single profile; rather, there are high-energy bands spreading wavenumber-wise. Therefore, we allow for a certain range (solid black curves in Figure 2) enclosing each dispersion relation curve. By visual inspection, the lower (upper) limit wavenumber of the bounding range is set to be below (above) that from the red curve by 7×10^{-3} (9×10^{-3}) cpkm; wherever the upper limit of mode-1 IGWs exceeds the lower limit of mode-2 IGWs, the average is taken to be the boundary. A similar idea of using the dispersion relation at a specific frequency was applied to extract coherent tidal SSH from altimetric or model data, where the wavenumber band was also subjectively determined by trial and error (Dushaw, 2015) or through adding/subtracting an offset (Zhao et al., 2019) like our treatment here. It is challenging to objectively define the range bounding each dispersion relation curve (Dushaw, 2015) somewhat because it is difficult to simultaneously take the nonuniform stratification and background currents into account. Under such circumstances, the subjective method could be a convenient and effective choice. Our ad hoc selection of the bounding band for each mode will be justified to perform well in Section 4. Mode-3 IGWs could have been extracted similarly, but the obtained horizontal velocities were not dynamically consistent with the extracted SSH according to internal wave dynamics (see Figure S1 in Supporting Information S1). This

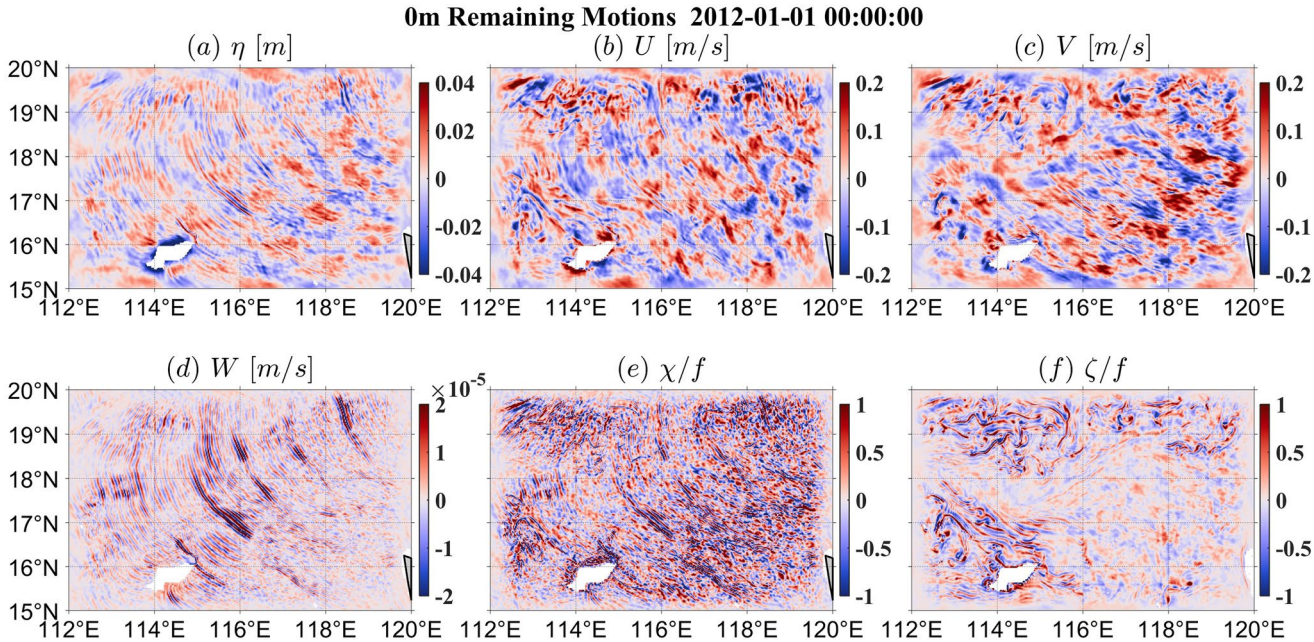

Figure 4. The remaining signal, after low-mode internal gravity waves and mesoscale motions are extracted, for (a) sea surface height, (b) zonal velocity, (c) meridional velocity, (d) vertical velocity, (e) horizontal divergence scaled by the local Coriolis parameter f, and (f) relative vorticity scaled by the local Coriolis parameter f.

probably implies that the spatiotemporal overlap between IGWs and submesoscale flows (e.g., McWilliams, 2016) becomes significant starting from this mode, weakening the effectiveness of using the dispersion relations to constrain IGWs at these scales. We hence define the first two modes as *low-mode* IGWs and the rest as *high-mode* IGWs. The low-mode IGWs ($\widehat{\eta_{Lwave}}$; ^ denotes the Fourier transform with respect to x, y, and t; thus all variables with ^ are functions of (k, l, ω) which denotes the zonal wavenumber, meridional wavenumber and frequency, respectively) are first extracted from the modified full flow (i.e., $\widehat{\eta_{mFull}}$) in spectral space according to the banded dispersion relation curves, and then their physical fields (η_{Lwave}) are recovered via inverse Fourier transform. For the extraction of high-mode IGWs, other dynamical constraints are required.

3.3. Extracting Mesoscale Motions

The mesoscale motions are marked in Figure 2. The oceanic mesoscale is regarded here as sub-inertial flows with horizontal scales above the first baroclinic deformation radius R_d. Once the low-mode IGWs $\widehat{\eta_{Lwave}}$ are extracted from $\widehat{\eta_{mFull}}$, the remainder, that is, $\widehat{\eta_{mFull}} - \widehat{\eta_{Lwave}}$, is lowpass-filtered both in time and space to extract the mesoscale flow $\widehat{\eta_{Meso}}$, where the cutoff period and wavelength are set to be 46.2 hr (i.e., the inertial period at the southern edge of the study region) and 50 km (roughly the minimal R_d of the study region), respectively.

3.4. Separating High-Mode IGWs and Submesoscale Motions

Once low-mode IGWs and the mesoscale are extracted, the remaining SSH variability, namely $\widehat{\eta_{Remn}} = \widehat{\eta_{mFull}} - \widehat{\eta_{Lwave}} - \widehat{\eta_{Meso}}$, is due to high-mode IGWs and submesoscale flows, and thus has both wavy and vortical features as indicated by the evident propagating features in the horizontal divergence field and the strong vorticity filaments in the relative vorticity field, respectively (Figure 4). It is still an unresolved issue to separate high-mode IGWs and submesoscale motions (McWilliams, 2016) partly due to the overlaps in time and space scales of these wavy and vortical motions. Obviously, the overlaps invalidate the utility of the dispersion relation or simple temporal-spatial filtering to carry out further decomposition solely based on SSH data. In the following, additional dynamical constraints are invoked to distinguish high-mode IGWs from submesoscale motions, both of which can only be roughly indicated in Figure 2.

The governing equations of large-scale currents, barotropic tides, low-mode IGWs and mesoscale flows are approximately known. They can be removed from the momentum equation for the full flow and the left terms

should govern the evolution of the remaining motions. As an example, consider the zonal momentum equation of the full flow

$$\frac{\partial u}{\partial t}+u\frac{\partial u}{\partial x}+v\frac{\partial u}{\partial y}+w\frac{\partial u}{\partial z}-f_0 v=-\frac{1}{\rho_0}\frac{\partial p}{\partial x}+\frac{\partial}{\partial z}\left(A_z\frac{\partial u}{\partial z}\right) \tag{1}$$

where $\boldsymbol{u}=(u,v,w)$ is the velocity associated with the full flow, f_0 is the Coriolis parameter, ρ_0 is the reference density and p is the pressure, A_z is the vertical viscosity coefficient. Rewrite $\boldsymbol{u}$ and p as follows

$$\begin{cases}\boldsymbol{u}=\boldsymbol{u}_{\text{Wave}}+\boldsymbol{u}_{\text{Geo}}+\boldsymbol{u}_{\text{Ekman}}+\boldsymbol{u}_{\text{Remn}}\\ p=p_{\text{Wave}}+p_{\text{Geo}}+p_{\text{Ekman}}+p_{\text{Remn}}\end{cases} \tag{2}$$

where the subscript Wave denotes barotropic tides and low-mode IGWs, Geo stands for mesoscale flows plus the geostrophic component of large-scale currents, Ekman represents the Ekman component of large-scale currents. Recall that p_{Ekman} is zero and will be omitted hereafter. Approximately, with the assumption that waves and background flows have similar horizontal scales (Kunze, 1985), Wave is governed by linear wave dynamics which additionally includes the straining and Doppler shift (Kunze, 1985); assuming that other flow components do not significantly influence its evolution, Geo satisfies the QG dynamics which is commonly used to explore meso- and large-scale geostrophic circulations; Ekman is in the well-known Ekman balance which assumes that the self-interaction (i.e., $u_{\text{Ekman}}\frac{\partial u_{\text{Ekman}}}{\partial x}+v_{\text{Ekman}}\frac{\partial u_{\text{Ekman}}}{\partial y}+w_{\text{Ekman}}\frac{\partial u_{\text{Ekman}}}{\partial z}$) and the cross-interaction with Geo (i.e., $u_{\text{Ekman}}\frac{\partial u_{\text{Geo}}}{\partial x}+v_{\text{Ekman}}\frac{\partial u_{\text{Geo}}}{\partial y}+w_{\text{Ekman}}\frac{\partial u_{\text{Geo}}}{\partial z}+u_{\text{Geo}}\frac{\partial u_{\text{Ekman}}}{\partial x}+v_{\text{Geo}}\frac{\partial u_{\text{Ekman}}}{\partial y}+w_{\text{Geo}}\frac{\partial u_{\text{Ekman}}}{\partial z}$) are negligible, but additionally includes the time derivative term to take the slow temporal variation into consideration. Therefore, the following equations approximately hold

$$\begin{cases}\begin{aligned}&\frac{\partial u_{\text{Wave}}}{\partial t}+u_{\text{GE}}\frac{\partial u_{\text{Wave}}}{\partial x}+v_{\text{GE}}\frac{\partial u_{\text{Wave}}}{\partial y}+w_{\text{GE}}\frac{\partial u_{\text{Wave}}}{\partial z}\\ &\quad+u_{\text{Wave}}\frac{\partial u_{\text{GE}}}{\partial x}+v_{\text{Wave}}\frac{\partial u_{\text{GE}}}{\partial y}+w_{\text{Wave}}\frac{\partial u_{\text{GE}}}{\partial z}\\ &\quad+u_{\text{Wave}}\frac{\partial u_{\text{Wave}}}{\partial x}+v_{\text{Wave}}\frac{\partial u_{\text{Wave}}}{\partial y}+w_{\text{Wave}}\frac{\partial u_{\text{Wave}}}{\partial z}-f_0 v_{\text{Wave}}=-\frac{1}{\rho_0}\frac{\partial p_{\text{Wave}}}{\partial x}\\ &\frac{\partial u_{\text{Geo}}}{\partial t}+u_{\text{Geo}}\frac{\partial u_{\text{Geo}}}{\partial x}+v_{\text{Geo}}\frac{\partial u_{\text{Geo}}}{\partial y}+w_{\text{Geo}}\frac{\partial u_{\text{Geo}}}{\partial z}-f_0 v_{\text{Geo}}=-\frac{1}{\rho_0}\frac{\partial p_{\text{Geo}}}{\partial x}\\ &\frac{\partial u_{\text{Ekman}}}{\partial t}-f_0 v_{\text{Ekman}}=\frac{\partial}{\partial z}\left(A_z\frac{\partial u_{\text{Ekman}}}{\partial z}\right)\approx\frac{\partial}{\partial z}\left(A_z\frac{\partial u}{\partial z}\right)\end{aligned}\end{cases} \tag{3}$$

where GE denotes Geo + Ekman, $u_{\text{Wave}}\frac{\partial u_{\text{GE}}}{\partial x}+v_{\text{Wave}}\frac{\partial u_{\text{GE}}}{\partial y}+w_{\text{Wave}}\frac{\partial u_{\text{GE}}}{\partial z}$ denotes the straining and $u_{\text{GE}}\frac{\partial u_{\text{Wave}}}{\partial x}+v_{\text{GE}}\frac{\partial u_{\text{Wave}}}{\partial y}+w_{\text{GE}}\frac{\partial u_{\text{Wave}}}{\partial z}$ denotes the Doppler shift. Here the assumption that Ekman contributes dominantly to the viscous term is reasonably made. Subtracting the equation set 3 from Equation 1 gives

$$\begin{aligned}&\frac{\partial u_{\text{Remn}}}{\partial t}+u_{\text{Remn}}\frac{\partial u_{\text{Remn}}}{\partial x}+v_{\text{Remn}}\frac{\partial u_{\text{Remn}}}{\partial y}+w_{\text{Remn}}\frac{\partial u_{\text{Remn}}}{\partial z}\\ &\quad+u_{\text{Wave}}\frac{\partial u_{\text{Remn}}}{\partial x}+v_{\text{Wave}}\frac{\partial u_{\text{Remn}}}{\partial y}+w_{\text{Wave}}\frac{\partial u_{\text{Remn}}}{\partial z}\\ &\quad+u_{\text{Remn}}\frac{\partial u_{\text{Wave}}}{\partial x}+v_{\text{Remn}}\frac{\partial u_{\text{Wave}}}{\partial y}+w_{\text{Remn}}\frac{\partial u_{\text{Wave}}}{\partial z}\\ &\quad+u_{\text{GE}}\frac{\partial u_{\text{Remn}}}{\partial x}+v_{\text{GE}}\frac{\partial u_{\text{Remn}}}{\partial y}+w_{\text{GE}}\frac{\partial u_{\text{Remn}}}{\partial z}\\ &+u_{\text{Remn}}\frac{\partial u_{\text{GE}}}{\partial x}+v_{\text{Remn}}\frac{\partial u_{\text{GE}}}{\partial y}+w_{\text{Remn}}\frac{\partial u_{\text{GE}}}{\partial z}-f_0 v_{\text{Remn}}=-\frac{1}{\rho_0}\frac{\partial p_{\text{Remn}}}{\partial x}\end{aligned} \tag{4}$$

The interaction terms in Equation 4 can be respectively scaled as

$$\frac{U_{\text{Remn}}U_{\text{Remn}}}{L_{\text{Remn}}},\frac{U_{\text{Wave}}U_{\text{Remn}}}{L_{\text{Remn}}},\frac{U_{\text{Wave}}U_{\text{Remn}}}{L_{\text{Wave}}},\frac{U_{\text{GE}}U_{\text{Remn}}}{L_{\text{Remn}}},\frac{U_{\text{GE}}U_{\text{Remn}}}{L_{\text{GE}}} \tag{5}$$

As shown qualitatively in Figure 2 and quantitatively in Table 1, Remn generally has smaller horizontal scales, namely $L_{\text{Remn}}<L_{\text{Wave}}, L_{\text{Remn}}<L_{\text{GE}}$; GE generally has the largest magnitude and Remn is weakest, so

Table 1
Horizontal Centroid Wavelengths (km) of Different Variables Associated With Low-Mode IGWs, Mesoscale Motions and Remaining Motions

	η	U	V	W	χ	ζ
Low-mode IGWs	77.7	71.0	91.3	25.6	22.2	51.7
Mesoscale motions	236.8	156.4	144.8	145.2	66.7	80.0
Remaining motions	33.7	32.3	37.8	11.2	12.7	17.4

Note. Centroid wavelengths are the reciprocals of centroid wavenumbers which are in turn calculated as follows: $\frac{\iint K \cdot A(K,\omega)\, dK d\omega}{\iint A(K,\omega) dK\, d\omega}$, where $K = \sqrt{k^2 + l^2}$ and A represents the frequency-wavenumber spectra of any physical variable (e.g., U).

$U_{\text{Remn}} < U_{\text{Wave}} < U_{\text{GE}}$. Thus, the most significant term in Equation 5 is $\frac{U_{\text{GE}} U_{\text{Remn}}}{L_{\text{Remn}}}$. Correspondingly, Equation 4 can be approximated by

$$\frac{\partial u_{\text{Remn}}}{\partial t} + u_{\text{GE}} \frac{\partial u_{\text{Remn}}}{\partial x} + v_{\text{GE}} \frac{\partial u_{\text{Remn}}}{\partial y} + w_{\text{GE}} \frac{\partial u_{\text{Remn}}}{\partial z} - f_0 v_{\text{Remn}} = -\frac{1}{\rho_0} \frac{\partial p_{\text{Remn}}}{\partial x} \tag{6}$$

Therefore, the advection by the background flow, namely the Doppler shift $u_{\text{GE}} \frac{\partial u_{\text{Remn}}}{\partial x} + v_{\text{GE}} \frac{\partial u_{\text{Remn}}}{\partial y} + w_{\text{GE}} \frac{\partial u_{\text{Remn}}}{\partial z}$, exerts the strongest influence on the evolution of the remaining motions; other interaction terms are generally secondary. Note that this scenario is distinct from that discussed by Kunze (1985) where near-inertial and nonuniform geostrophic flows had similar horizontal scales and therefore both the Doppler shift and straining were important.

With the assumption that $(u_{\text{GE}}, v_{\text{GE}}, w_{\text{GE}})$ is spatially uniform and temporally constant, the linearized vorticity equation governing the remaining flow follows from the simplified momentum equation (e.g., Equation 6)

$$\frac{\partial \zeta_{\text{Remn}}}{\partial t} + u_{\text{GE}} \frac{\partial \zeta_{\text{Remn}}}{\partial x} + v_{\text{GE}} \frac{\partial \zeta_{\text{Remn}}}{\partial y} + w_{\text{GE}} \frac{\partial \zeta_{\text{Remn}}}{\partial z} + f_0 \chi_{\text{Remn}} = 0 \tag{7}$$

where ζ_{Remn} and χ_{Remn} are the relative vorticity and horizontal divergence of the remaining flow, respectively. Conventionally the vertical advection is ignored, giving

$$\frac{\partial \zeta_{\text{Remn}}}{\partial t} + u_{\text{GE}} \frac{\partial \zeta_{\text{Remn}}}{\partial x} + v_{\text{GE}} \frac{\partial \zeta_{\text{Remn}}}{\partial y} + f_0 \chi_{\text{Remn}} = 0 \tag{8}$$

The Fourier transform of Equation 8 is

$$i\omega \widehat{\zeta_{\text{Remn}}} + iku_{\text{GE}} \widehat{\zeta_{\text{Remn}}} + ilv_{\text{GE}} \widehat{\zeta_{\text{Remn}}} + f_0 \widehat{\chi_{\text{Remn}}} = i\Omega \widehat{\zeta_{\text{Remn}}} + f_0 \widehat{\chi_{\text{Remn}}} = 0 \tag{9}$$

where i is the imaginary unit and $\Omega = \omega + ku_{\text{GE}} + lv_{\text{GE}}$ denotes the intrinsic frequency. Similar to the classic normal-mode decomposition of the linearized primitive equations (Leith, 1980; Lien & Müller, 1992; P. Mülle r, 1984, 1988), the wavy mode is defined to have intrinsic frequencies above the inertial frequency, namely $|\Omega| > |f_0|$, whereas the vortical mode to have zero (lowest order) or much lower (higher-order correction) intrinsic frequencies, namely $|\Omega| \ll |f_0|$. Consequently, two important facts follow in *spectral* space from Equation 9: (a) the modulus of the horizontal divergence is larger than that of the relative vorticity for the wavy mode; (b) the modulus of the horizontal divergence is much smaller than that of the relative vorticity for the vortical mode.

Considering that each point in spectral space (i.e., (k, l, ω)) is contributed by a linear combination of the wavy and vortical modes (e.g., Bartello, 1995), the modulus of the horizontal divergence $|\widehat{\chi_{\text{Remn}}}|$ is expected to be larger (much smaller) than that of the relative vorticity $|\widehat{\zeta_{\text{Remn}}}|$ wherever the wavy (vortical) mode dominates. We currently cannot well tackle the complicated scenario where wavy and vortical modes are comparable in spectral magnitude. Therefore, high-mode IGWs and submesoscale flows, together comprising the remaining flows, can be defined as follows

$$\begin{cases} \widehat{\chi_{H\text{wave}}}(k,l,\omega) = \widehat{\chi_{\text{Remn}}}, \text{when } \left(|\widehat{\zeta_{\text{Remn}}}| < |\widehat{\chi_{\text{Remn}}}| \text{ and } |\Omega| > |f_0| \right) \text{at } (k,l,\omega) \\ \widehat{\zeta_{H\text{wave}}}(k,l,\omega) = \widehat{\zeta_{\text{Remn}}}, \text{when } \left(|\widehat{\zeta_{\text{Remn}}}| < |\widehat{\chi_{\text{Remn}}}| \text{ and } |\Omega| > |f_0| \right) \text{at } (k,l,\omega) \end{cases} \tag{10}$$

$$\begin{cases} \widehat{\chi_{\text{Submeso}}}(k,l,\omega) = \widehat{\chi_{\text{Remn}}}, \text{when } \left(|\widehat{\zeta_{\text{Remn}}}| > |\widehat{\chi_{\text{Remn}}}| \text{ or } |\Omega| < |f_0| \right) \text{at } (k,l,\omega) \\ \widehat{\zeta_{\text{Submeso}}}(k,l,\omega) = \widehat{\zeta_{\text{Remn}}}, \text{when } \left(|\widehat{\zeta_{\text{Remn}}}| > |\widehat{\chi_{\text{Remn}}}| \text{ or } |\Omega| < |f_0| \right) \text{at } (k,l,\omega) \end{cases} \tag{11}$$

where $\widehat{\zeta_{H\,\text{wave}}}$ ($\widehat{\chi_{H\,\text{wave}}}$) and $\widehat{\zeta_{\text{Submeso}}}$ ($\widehat{\chi_{\text{Submeso}}}$) are the relative vorticity (horizontal divergence) of high-mode IGWs and submesoscale flows, respectively. Hereafter, we simply ignore the constraints imposed by the intrinsic frequency Ω which is not known a priori.

Once the horizontal divergence and relative vorticity of high-mode IGWs (submesoscale flows) are known, the corresponding horizontal velocities can be inverted by solving the Poisson equations, just as in the classic Helmholtz decomposition. In practice, inverting the Poisson equations to obtain horizontal velocities in the present setting is equivalent to solving

$$\begin{cases} \widehat{\boldsymbol{u}_{H\,\text{wave}}}(k,l,\omega) = \widehat{\boldsymbol{u}_{\text{Remn}}}, \text{when } \left(|\widehat{\zeta_{\text{Remn}}}| < |\widehat{\chi_{\text{Remn}}}| \right) \text{at } (k,l,\omega) \\ \widehat{\boldsymbol{u}_{\text{Submeso}}}(k,l,\omega) = \widehat{\boldsymbol{u}_{\text{Remn}}}, \text{when } \left(|\widehat{\zeta_{\text{Remn}}}| > |\widehat{\chi_{\text{Remn}}}| \right) \text{at } (k,l,\omega) \end{cases} \tag{12}$$

where $\boldsymbol{u}_{\text{Remn}}$, $\boldsymbol{u}_{H\,\text{wave}}$, and $\boldsymbol{u}_{\text{Submeso}}$ are horizontal velocities of the remaining flows, high-mode IGWs, and submesoscale flows, respectively. This equivalence eliminates the necessity of solving the Poisson equation. More importantly, it allows us to readily decompose other variables like SSH of remaining flows in a similar manner

$$\begin{cases} \widehat{\eta_{H\,\text{wave}}}(k,l,\omega) = \widehat{\eta_{\text{Remn}}}, \text{when } \left(|\widehat{\zeta_{\text{Remn}}}| < |\widehat{\chi_{\text{Remn}}}| \right) \text{at } (k,l,\omega) \\ \widehat{\eta_{\text{Submeso}}}(k,l,\omega) = \widehat{\eta_{\text{Remn}}}, \text{when } \left(|\widehat{\zeta_{\text{Remn}}}| > |\widehat{\chi_{\text{Remn}}}| \right) \text{at } (k,l,\omega) \end{cases} \tag{13}$$

where $\widehat{\eta_{H\,\text{wave}}}$ and $\widehat{\eta_{\text{Submeso}}}$ are SSH of high-mode IGWs and submesoscale flows, respectively.

The decomposition based on Equations 12 and 13 is already acceptable except that frequency spectra of submesoscale flows artificially present peaks exactly at the four main tidal frequencies (K_1, O_1, M_2, S_2) (see Figure S2 in Supporting Information S1) due to the fact that our decomposition does not well tackle the scenario where the wavy and vortical modes have comparable spectral magnitudes. To remedy this, we modify Equations 12 and 13 to the following ones

$$\begin{cases} \widehat{\boldsymbol{u}_{H\,\text{wave}}}(k,l,\omega) = \widehat{\boldsymbol{u}_{\text{Remn}}}, \text{when } \left(|\widehat{\zeta_{\text{Remn}}}| < |\widehat{\chi_{\text{Remn}}}| \text{ or } (\omega = \omega_{\text{tide}}) \right) \text{at } (k,l,\omega) \\ \widehat{\eta_{H\,\text{wave}}}(k,l,\omega) = \widehat{\eta_{\text{Remn}}}, \text{when } \left(|\widehat{\zeta_{\text{Remn}}}| < |\widehat{\chi_{\text{Remn}}}| \text{ or } (\omega = \omega_{\text{tide}}) \right) \text{at } (k,l,\omega) \end{cases} \tag{14}$$

$$\begin{cases} \widehat{\boldsymbol{u}_{\text{Submeso}}}(k,l,\omega) = \widehat{\boldsymbol{u}_{\text{Remn}}}, \text{when } \left(|\widehat{\zeta_{\text{Remn}}}| > |\widehat{\chi_{\text{Remn}}}| \text{ and } (\omega \neq \omega_{\text{tide}}) \right) \text{at } (k,l,\omega) \\ \widehat{\eta_{\text{Submeso}}}(k,l,\omega) = \widehat{\eta_{\text{Remn}}}, \text{when } \left(|\widehat{\zeta_{\text{Remn}}}| > |\widehat{\chi_{\text{Remn}}}| \text{ and } (\omega \neq \omega_{\text{tide}}) \right) \text{at } (k,l,\omega) \end{cases} \tag{15}$$

where ω_{tide} are the frequencies of the four main tidal constituents, namely, K_1, O_1, M_2, S_2. Hereafter, Equations 14 and 15 are used to decompose the remaining flows.

In conclusion, based on the dynamical nature of each type of oceanic motions, we manage to decompose the full flow into large-scale currents, barotropic tides, low-mode IGWs, mesoscale flows, submesoscale flows, and high-mode IGWs. In the next section, we will analyze the decomposed flow components in detail, aiming to evaluate their dynamical consistency.

4. Results

4.1. Low-Mode IGWs

Low-mode IGWs are defined to be mode-1 and mode-2 IGWs which are extracted according to their dispersion relations. Figure 5 is a snapshot of the extracted low-mode IGWs shown in terms of various dynamical variables. The southwestward-propagating wave pattern can be easily identified in all the variables, in agreement with

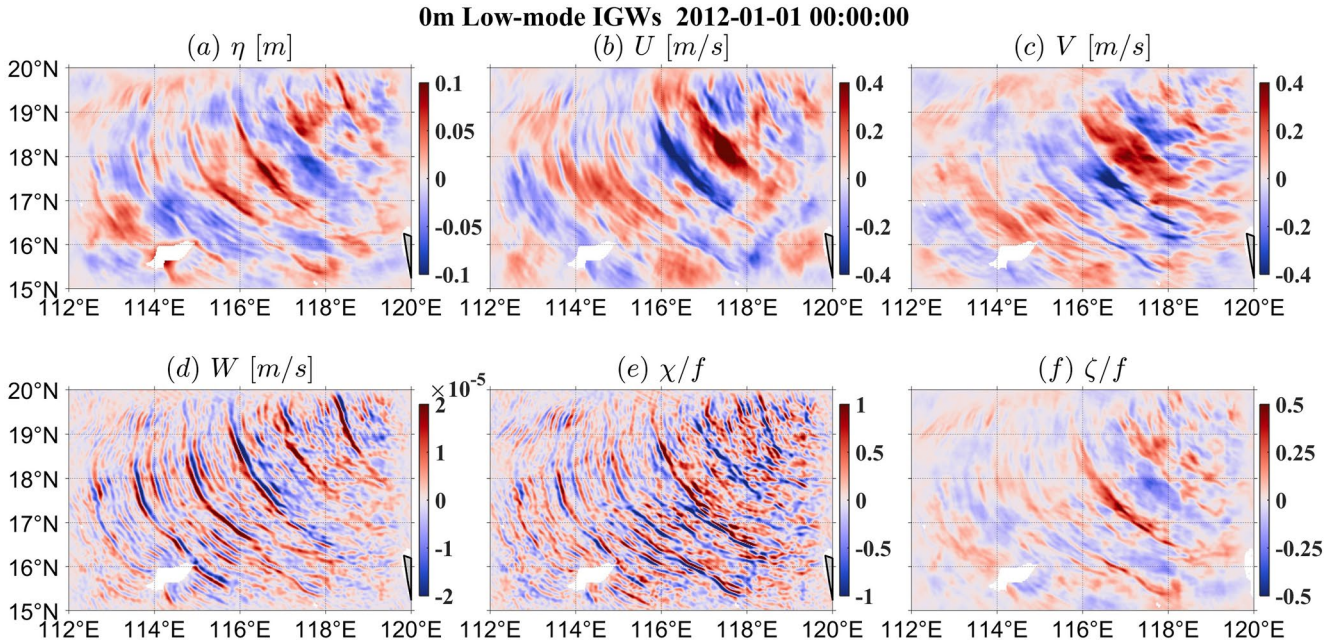

Figure 5. Same as Figure 4 but for low-mode internal gravity waves.

altimeter-based observations (Zaron, 2019; Zhao, 2014). Visually, the dominant spatial scale of the relative vorticity is smaller than that of SSH and horizontal velocities. This is confirmed by the distinct centroid wavelengths (51.7 vs. 71.0–91.3 km) in Table 1, where the centroid wavelength is taken as the mean wavelength weighted by the wavenumber spectral density. This is because spatial derivatives of horizontal velocities have larger contributions from high-wavenumber features, as is common for most multiscale flows like two-dimensional turbulence. Interestingly, the horizontal divergence is dominated by even finer scales (22.2 km), which can be explained by considering the linearized equation for the relative vorticity,

$$\frac{\partial \zeta_{L\text{wave}}}{\partial t} = -f_0 \chi_{L\text{wave}} \tag{16a}$$

where $\chi_{L\text{wave}}$ and $\zeta_{L\text{wave}}$ are the horizontal divergence and relative vorticity of low-mode IGWs, respectively. The Fourier transform of Equation 16a gives

$$\widehat{\chi_{L\text{wave}}} = -\frac{i\omega\widehat{\zeta_{L\text{wave}}}}{f_0} \tag{16b}$$

It is clear from Equation 16b that the horizontal divergence is more contributed by high-frequency signals compared with the relative vorticity, which in turn results in finer spatial scales according to the following dispersion relation

$$\omega^2 = {f_0}^2 + c_n^2\left(k^2 + l^2\right) \tag{17}$$

where c_n (the eigenvalue) is the phase speed of the n-th baroclinic mode of gravity waves (e.g., Majda, 2003; Pedlosky, 2003). Note also that the continuity equation relates the horizontal divergence to the vertical velocity. As such, by taking vertical integration of the continuity equation followed by the conventional variable separation for linear IGWs, the surface vertical velocity due to low-mode IGWs can be calculated as follows

$$\begin{aligned} & w_{L\text{wave}}(x, y, \eta, t) \\ & = w_{L\text{wave}}(x, y, -H, t) - \int_{-H}^{\eta} \chi_{L\text{wave}}(x, y, z, t) dz \\ & = w_{L\text{wave}}(x, y, -H, t) - \chi_h(x, y, t) \int_{-H}^{\eta} \chi_v(z) dz \end{aligned} \tag{18}$$

where $w_{L\text{wave}}(x, y, \eta, t)$ and $w_{L\text{wave}}(x, y, -H, t)$ are the vertical velocity of low-mode IGWs at the sea surface $z = \eta$ and at the bottom $z = -H$, respectively, and $\chi_{L\text{wave}}$ is the product of the horizontally varying part $\chi_h(x, y, t)$ and the vertically varying part $\chi_v(z)$. Given $w_{L\text{wave}}(x, y, -H, t)$, the horizontal scale of the vertical velocity is completely determined by the horizontally varying part of the horizontal divergence. This explains why the spatial patterns (including scales) of the vertical velocity and horizontal divergence generally resemble each other for IGWs.

We now examine the dynamical consistency among physical variables for low-mode IGWs quantitatively. The interaction terms (e.g., advection by the background flow) in the momentum equation surely affect the dynamics of low-mode IGWs, but remain difficult to quantify. Zaron (2019) parameterized such effects by a linear damping term, but choosing an appropriate damping time scale is not trivial. As a compromise, we assume no damping, which is equivalent to considering the linearized dynamics of IGWs. Separation of variables reduces the linearized primitive equations to infinite shallow water systems (i.e., infinite number of vertical normal modes) with differing equivalent depths (Majda, 2003; Pedlosky, 2003). Using SSH for the first two modes of IGWs, surface horizontal velocities can be derived straightforwardly according to the following polarization relations (e.g., Gill, 1982)

$$\begin{cases} \widehat{u_{L\text{wave}}} = \dfrac{g(ilf - \omega k)}{\omega^2 - {f_0}^2}\widehat{\eta_{L\text{wave}}} \\ \widehat{v_{L\text{wave}}} = -\dfrac{g(ikf + \omega l)}{\omega^2 - {f_0}^2}\widehat{\eta_{L\text{wave}}} \end{cases} \tag{19}$$

where $\left(\widehat{u_{L\text{wave}}}, \widehat{v_{L\text{wave}}}\right)$ is the surface velocities of low-mode IGWs and g is the acceleration due to gravity. Figure 6 shows the zonal velocities derived from the decomposed SSH for low-mode IGWs, together with the corresponding correlation and root mean square (RMS) errors between the derived velocities and the directly decomposed ones. Overall, these independent estimates show remarkable consistency in terms of the velocity magnitude and pattern. Almost all of the region has RMS errors smaller than 0.04 (0.06) m/s for mode-1 (mode-2) IGWs, which are negligible in comparison with the typical magnitude of directly decomposed velocities. This high consistency also holds for the spatial pattern and temporal evolution as indicated by the extremely high correlations over the entire domain for the simulation period. Visible discrepancies only occur near the edges of the study region due to the windowing effect and around the island probably due to the interpolation/extrapolation or abrupt changes in background dynamical conditions (e.g., stratification) when approaching the island. Analysis of the meridional velocity gives very similar results and is thus not presented.

4.2. Mesoscale Flows

As already mentioned, mesoscale flows refer to flows with horizontal scales larger than the first baroclinic deformation radius and frequencies lower than the inertial frequency. The decomposed mesoscale flows at the surface are shown in Figure 7. As anticipated, SSH is dominated by relatively large-scale structures with a centroid wavelength of 236.8 km. The dominating scales of zonal (156.4 km) and meridional (144.8 km) velocities are smaller than that of SSH due to the spatial derivatives through geostrophic balance. For mesoscale flows, a similar relation like Equation 16 does not exist and the scales of relative vorticity and horizontal divergence (80.0 vs. 66.7 km) seem to be quite similar. Both are smaller than the scale of horizontal velocities due to the highpass-filtering nature of spatial differentiation, as explained above. In striking contrast to the low-mode IGWs, the mesoscale vertical velocity has almost the same dominating spatial scale (145.2 km) as horizontal velocities, as a result of the balanced dynamics. Essentially, mesoscale flows can be described by the QG theory. Then, for mesoscale flows, Equation 18 is reduced to the relation between the vertical velocity and ageostrophic (rather than geostrophic) horizontal velocities and does not provide an obvious explanation for the observed scale similarity of the vertical and geostrophic horizontal velocities. Instead, the relevant equation is now due to the kinematic boundary condition of the QG flow at the surface,

$$\widehat{w_{\text{Meso}}} = i\omega\widehat{\eta_{\text{Meso}}} \tag{20}$$

where $\widehat{w_{\text{Meso}}}$ and $\widehat{\eta_{\text{Meso}}}$ are surface vertical velocity and SSH of mesoscale flows, respectively. Similar to the physical reasoning for low-mode IGWs discussed above, the mesoscale vertical velocity contains more significant high-frequency variabilities than mesoscale SSH. According to the frequency-wavenumber spectra of SSH shown in Figure 2, high-frequency mesoscale signals tend to have high wavenumbers (e.g., Arbic et al., 2014; Liang, 2016; Torres et al., 2018). Therefore, the time derivative of SSH in Equation 20 can roughly be equivalently

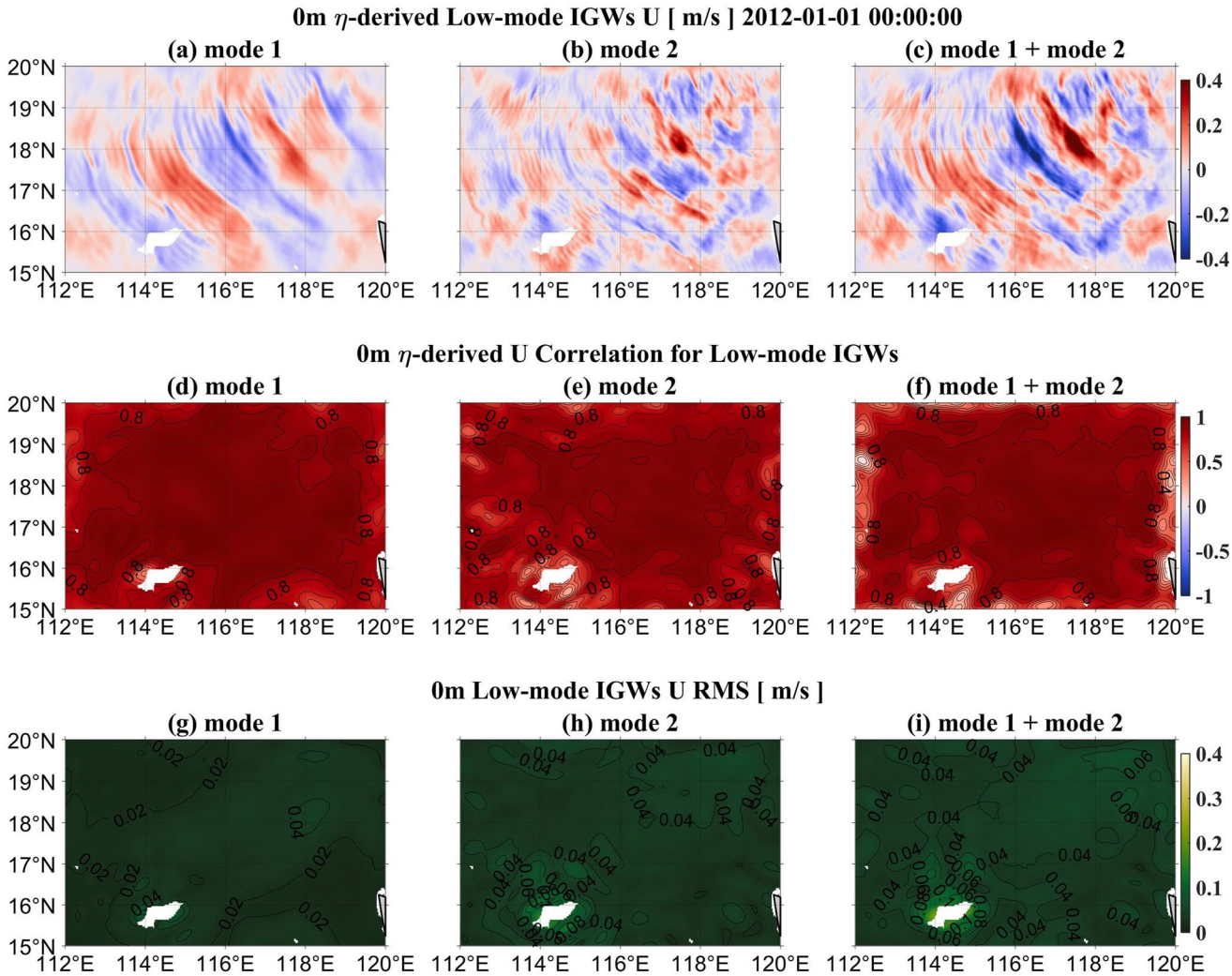

Figure 6. Surface zonal velocity derived from the decomposed sea surface height for low-mode internal gravity waves (IGWs) (a–c), the pointwise correlations over the simulation period between derived and directly decomposed velocities of low-mode IGWs (d–f) and the root mean square error over the simulation period between the derived and the directly decomposed (g–i). The left (a, d, and g), middle (b, e, and h), and right (c, f, and i) columns show mode-1 IGWs, mode-2 IGWs and their sum, respectively.

converted to the space derivative of SSH. As a result, the mesoscale vertical velocity is characterized by smaller dominant horizontal scales than SSH and coincides with the horizontal scales of horizontal velocities which are in turn derived from SSH via the geostrophic balance. The obvious separation in the dominating scale of vertical velocity between low-mode IGWs and mesoscale motions (25.6 vs. 145.2 km) provides the dynamical basis for the flow decomposition via spatial filtering adopted by Sugimoto and Plougonven (2016).

As a quantitative examination, surface horizontal velocities associated with mesoscale flows are derived from SSH according to the geostrophic balance,

$$\begin{cases} \widehat{u_{\text{Meso}}} = -\dfrac{igl}{f_0}\widehat{\eta_{\text{Meso}}} \\ \widehat{v_{\text{Meso}}} = \dfrac{igk}{f_0}\widehat{\eta_{\text{Meso}}} \end{cases} \tag{21}$$

where $\left(\widehat{u_{\text{Meso}}}, \widehat{v_{\text{Meso}}}\right)$ is the mesoscale velocity at the surface. Figure 8 displays the snapshot of the derived horizontal velocities which qualitatively resemble that of directly decomposed ones in Figure 7. Quantitatively, the derived horizontal velocities well capture both the spatial pattern and temporal evolution of the decomposed mesoscale flows, indicated by the high correlation over nearly the whole domain except for the peripheries due

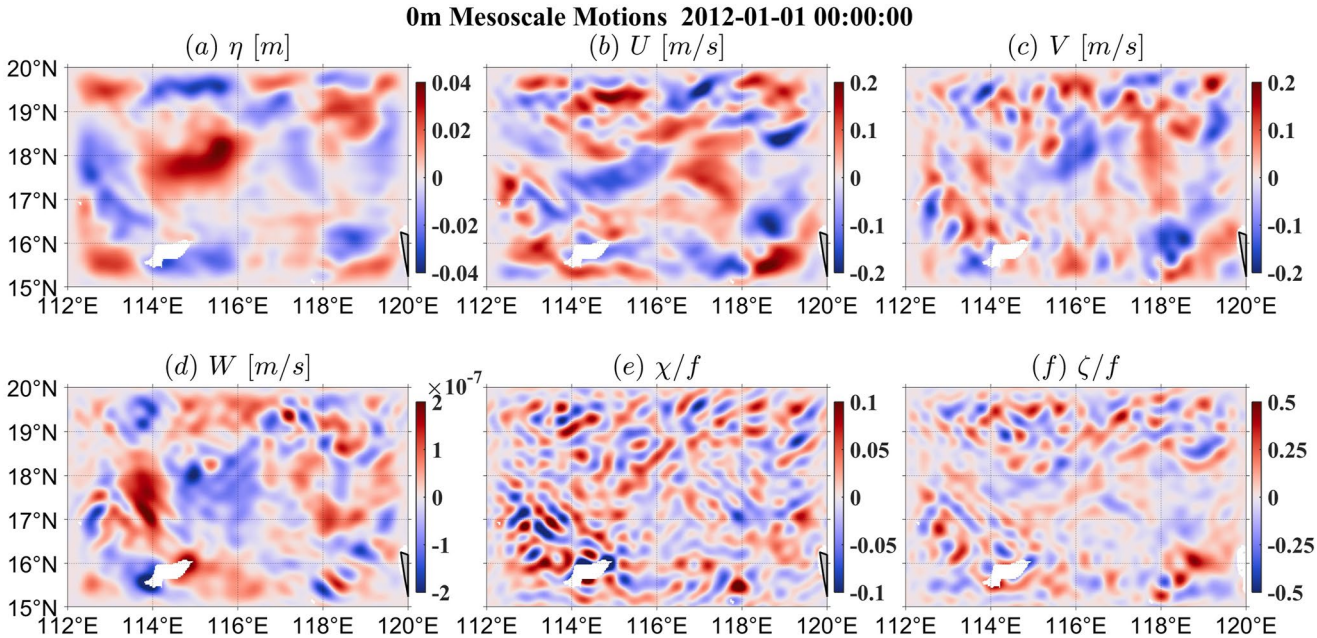

Figure 7. Same as Figure 4 but for mesoscale motions.

to the windowing effect of the Fourier transform and a zonally elongated stripe between 15° and 16°N for zonal velocity due to the presence of the island (Figure 8). The RMS errors for zonal (meridional) velocity are smaller than 0.08 (0.04) m/s in most parts of the study region excluding the effects of the island and windowing, which is satisfactorily low compared with the typical magnitude (~0.2 m/s) of directly decomposed mesoscale velocities.

In our study region, SSH and horizontal velocities associated with low-mode IGWs are nearly two times larger in magnitude than their respective counterparts associated with mesoscale flows. This is because this region is

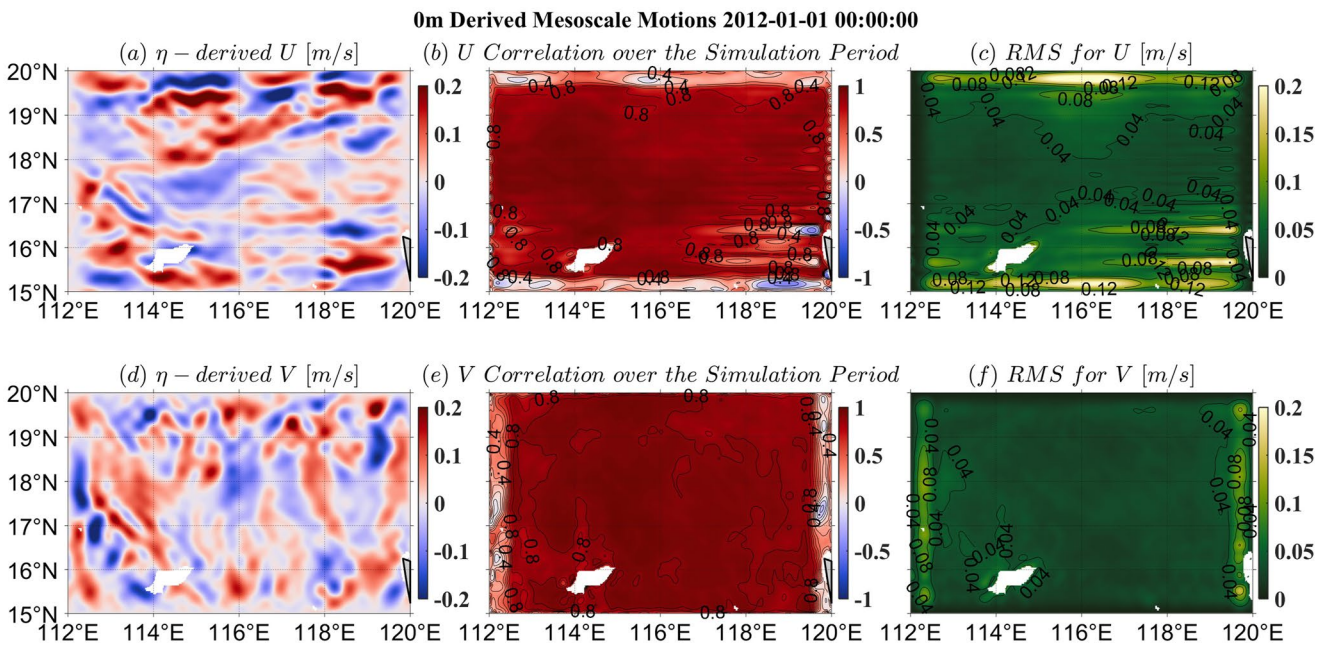

Figure 8. Surface zonal velocity and meridional velocity derived from the decomposed sea surface height for mesoscale motions (a, d), the pointwise correlations over the simulation period between derived and directly decomposed mesoscale velocities (b, e) and the root mean square error over the simulation period between the derived and the directly decomposed (c, f).

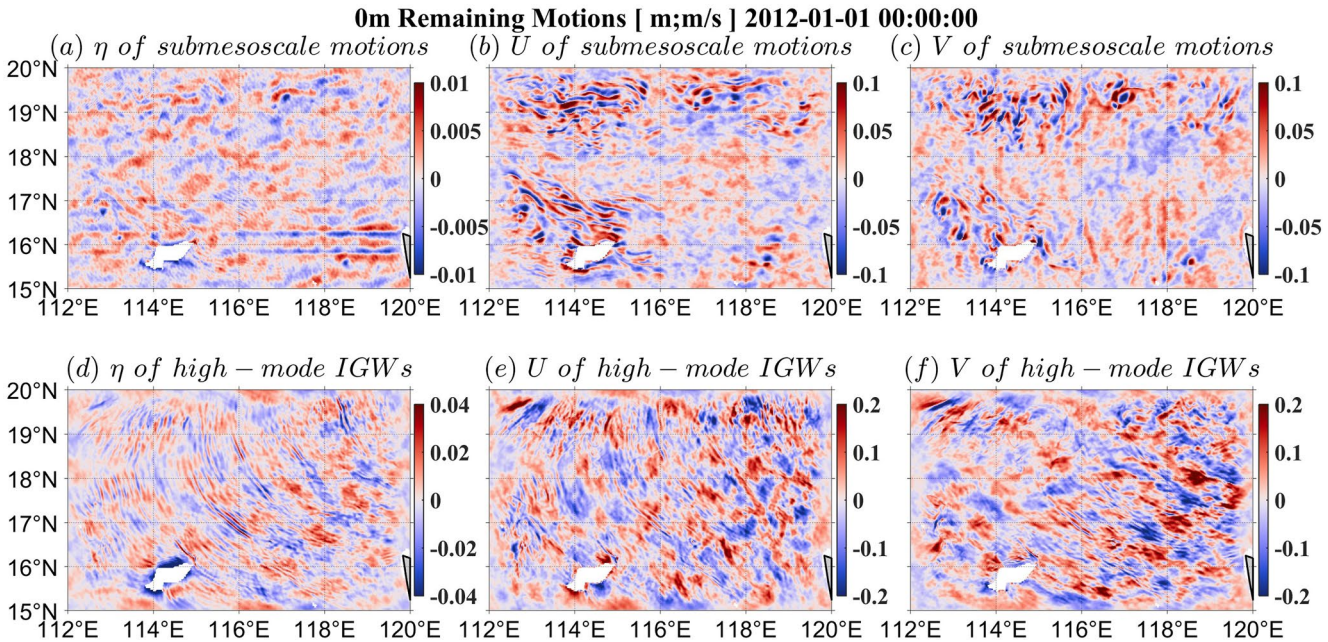

Figure 9. A snapshot of (a, d) sea surface height, (b, e) zonal velocity, and (c, f) meridional velocity due to the (a–c) decomposed submesoscale motions and (d–f) high-mode internal gravity waves.

characterized by relatively weak mesoscale flows (Cheng & Qi, 2010) and strong internal tides (Zhao, 2014). Moreover, compared to low-mode IGWs, the vertical velocity and horizontal divergence of mesoscale flows are two and one orders of magnitude weaker, respectively.

4.3. Submesoscale Flows and High-Mode IGWs

Submesoscale flows are defined to be vortical motions with horizontal scales smaller than the first baroclinic deformation radius. High-mode IGWs are defined as IGWs excluding the first and second modes. Figure 9 shows a snapshot of SSH, zonal and meridional velocities for the decomposed submesoscale flows and high-mode IGWs while the corresponding relative vorticity and horizontal divergence are displayed in Figure 10. Obviously, the wavy feature of high-mode IGWs variables resembles that of low-mode IGWs. Submesoscale SSH and horizontal velocities are characterized by filaments and eddies, which are more readily identifiable from the relative vorticity (highlighted by green and black boxes, respectively). Importantly, the submesoscale horizontal divergence is also significant, especially along filaments. The horizontal kinetic energy spectra at the surface (Figure 11) demonstrate that submesoscale flows are predominant in terms of energy level at sub-inertial frequencies whereas high-mode IGWs are mostly predominant at super-inertial frequencies. Around the inertial frequency, their energy levels are generally comparable. We consider our separation of the submesoscale flows from high-mode IGWs as satisfactory given the challenging nature of such a separation.

In summary, after removing large-scale currents and barotropic tides, we have managed to decompose the flows into low-mode IGWs, mesoscale flows, high-mode IGWs, and submesoscale flows and have shown that the decomposed components reveal expected dynamical characteristics.

5. Discussion

We have demonstrated that the full flow field can be decomposed by virtue of their respective dynamics. For completeness of analysis, some additional aspects are discussed below.

5.1. Ray Tracing

We extract low-mode IGWs following a band enveloping each dispersion relation curve, as depicted in Figure 2. The mechanism for the wavenumber-wise spreading of spectral energies along a specific frequency requires a

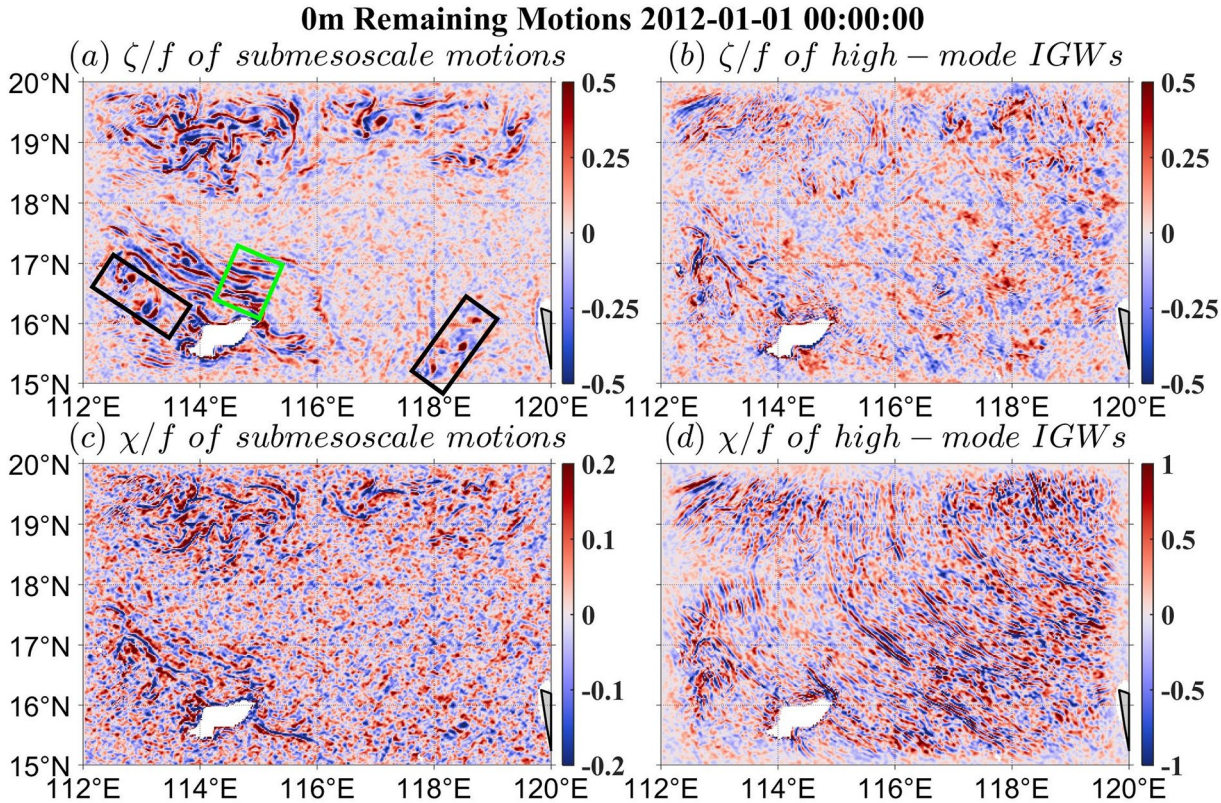

Figure 10. The relative vorticity (a, b) scaled by the local Coriolis parameter f and horizontal divergence (c, d) scaled by the local Coriolis parameter due to submesoscale motions (a, c) and high-mode internal gravity waves (b, d). The green and black boxes in panel (a) highlight submesoscale filaments and eddies, respectively.

physical interpretation. To this end, the two-dimensional ray-tracing method is used to examine the effect of the large-scale currents and horizontally varying background stratification. Suppose that the background stratification and large-scale currents do not vary with time, it follows that wave frequencies remain constant if traced with the group velocity. Then the wavenumber vector $\boldsymbol{k} = (k, l)$ and the position evolution of the corresponding raypath $\boldsymbol{x} = (x, y)$ are governed by (e.g., Bühler, 2009),

$$\begin{cases} \dfrac{d\boldsymbol{x}}{dt} = \dfrac{\partial \Omega}{\partial \boldsymbol{k}} \\ \dfrac{d\boldsymbol{k}}{dt} = -\dfrac{\partial \Omega}{\partial \boldsymbol{x}} \end{cases} \tag{22}$$

where $\Omega = \boldsymbol{U}(\boldsymbol{x}) \cdot \boldsymbol{k} + \omega(\boldsymbol{k}(\boldsymbol{x}, t), \boldsymbol{x})$ is the intrinsic frequency, $\boldsymbol{U}(\boldsymbol{x})$ is the temporal mean of the full flow (u, v) and $\omega = \pm\sqrt{f_0^2 + c_n^2 K^2}$ is the absolute frequency with c_n (c_1 shown in Figure 1a and c_2 in Figure 1b) denoting the same as in Equation 17.

Considering the dominant wavy pattern propagating from the northeast, as mentioned in Section 4.1, we initiate 10 rays around the northeastern corner. For each ray, three frequencies (K_1, M_2, 0.4 cph) of mode-1 and mode-2 IGWs are traced for 1 day. The evolution of ray paths is overlaid on SSH of the decomposed low-mode IGWs (Figure 12). It is clear that the refracted rays agree with the propagation of SSH, consistent with the controlling effect of the background flow and stratification on the propagation of low-mode IGWs. Meanwhile, wavenumbers change continuously at traced frequencies (white dots shown in Figure 2) due to the presence of background flows and

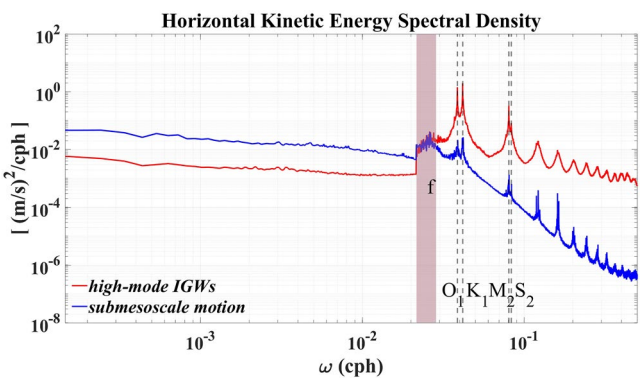

Figure 11. The horizontal kinetic energy frequency spectra associated with submesoscale motions (blue curve) and high-mode internal gravity waves (red curve) at the sea surface. The wavenumber spectra are obtained through frequency-wise integration of corresponding frequency-wavenumber spectra like Figure 2.

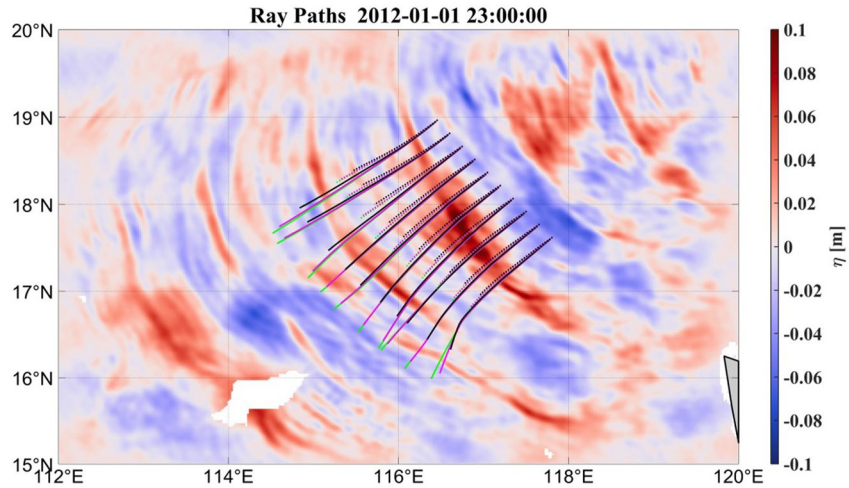

Figure 12. Sea surface height of the decomposed low-mode internal gravity waves (IGWs) overlaid with ray paths. Solid curves indicate ray paths of mode-1 IGWs while dashed curves show those of mode-2 IGWs. Black, magenta, and green curves indicate ray paths with frequencies of K_1, M_2, and 0.4 cph, respectively.

the horizontally inhomogeneous stratification. This, to some extent, justifies our selection of the enveloping bands along the dispersion relation curves to represent low-mode IGWs. Note that M. Müller et al. (2015) and Savage, Arbic, Alford, et al. (2017) plotted bounding dispersion relation curves for IGWs according to the maximal and minimal c_n along the northern and southern edges of their study regions. The results of our ray-tracing experiments provide a physical explanation for their selection of bounding curves. We would like to emphasize additionally, however, that their bounding curves did not consider the effect of the background flow.

5.2. Influence of Aliasing

The horizontal grid spacing, time-marching step and outputting time interval of the LLC4320 simulation are ∼2 km, 25 s and 1 hr, respectively. As shown by C. Wang et al. (2022), the grid spacing is the limiting factor in resolving IGWs according to the dispersion relation of mode-1 IGWs. Thus, the fastest IGWs possibly resolved by the LLC4320 simulation have a period of 24 min with a wavelength of ∼4 km. With the model simulation stored hourly, IGWs with a period greater than 24 min and less than the Nyquist period of 2 hr are inevitably aliased. The aliasing is clearly present in Figure 2 where spectral energies of low-mode IGWs fold back after reaching the highest frequency (i.e., 0.5 cph). Such aliasing, which has been pointed out by Savage, Arbic, Alford, et al. (2017) and Qiu et al. (2019) and quantified by C. Wang et al. (2022), poses great difficulties to the separation of high-mode IGWs from submesoscale motions.

When a signal with a certain period is inadequately sampled, the spectral energy peak survives but is aliased to a lower frequency. To be precise, aliasing mainly changes the location of a signal in frequency space and generally leaves such physical properties as the relative magnitude of the horizontal divergence and relative vorticity unchanged. Thus, it seems natural that our approach of distinguishing high-mode IGWs from submesoscale motions would handle the effect of aliasing. This is indeed confirmed by the results of the decomposition. As shown by SSH frequency-wavenumber spectra (Figure 13), the aliased IGWs (i.e., the spectral energy folding) are well recovered as high-mode IGWs (Figure 13a). Although some are unfortunately attributed to submesoscale motions (Figure 13b), most aliased IGWs are satisfactorily extracted (Figure 13c). Similar results are revealed by the horizontal kinetic energy frequency-wavenumber spectra (not shown). It can thus be concluded that the proposed decomposition can naturally take the effect of aliasing into consideration.

5.3. Comparison With Lagrangian Filtering

Analysis in Section 4 demonstrates that the decomposed variables are dynamically consistent in both qualitative and quantitative sense. It would be more informative to compare our decomposition methodology with Lagrangian filtering which has recently gained much popularity in the decomposition of oceanic flows. The recently released

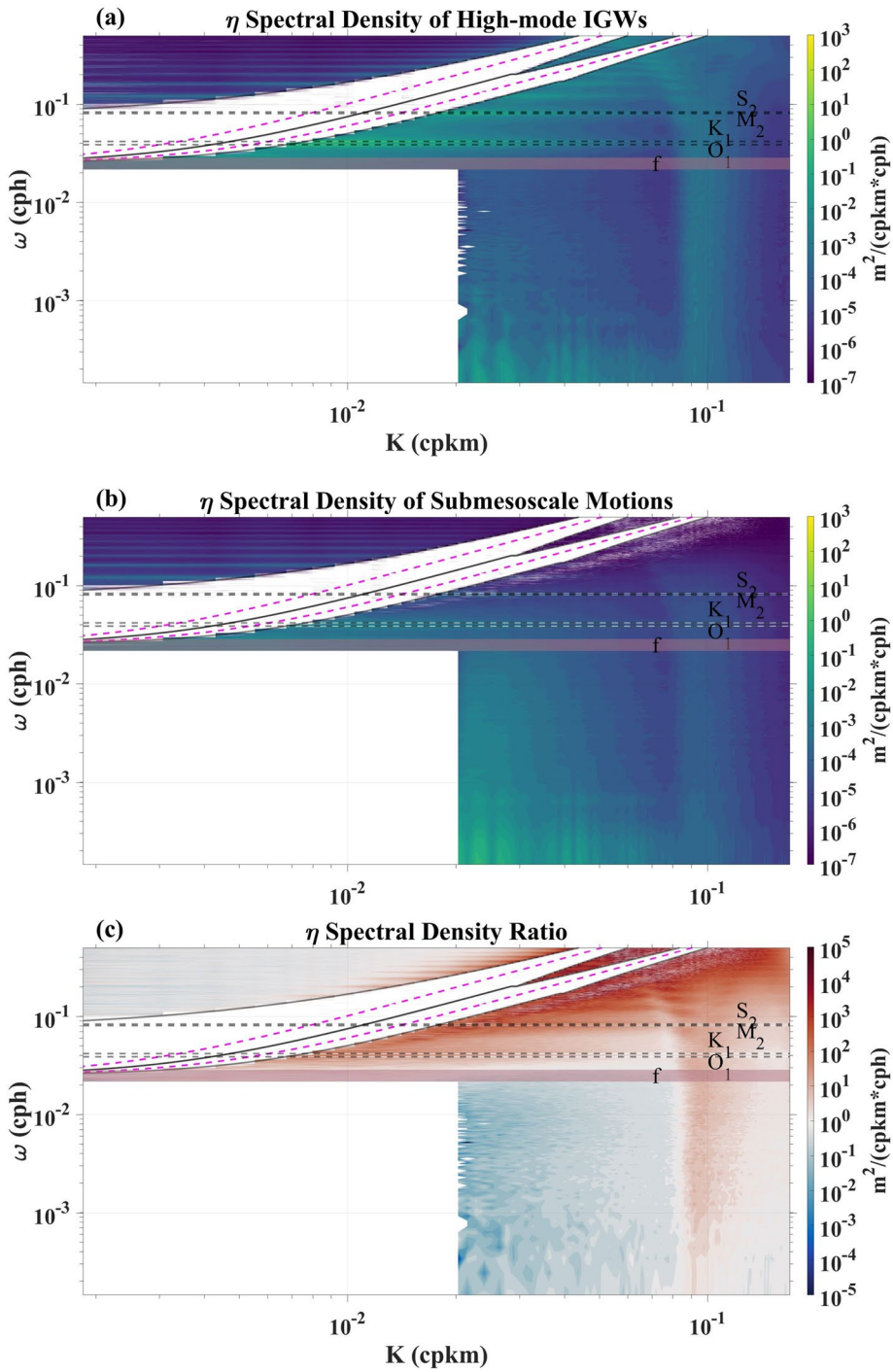

Figure 13. The frequency-wavenumber spectral density of sea surface height associated with (a) high-mode internal gravity waves and (b) submesoscale motions and the spectral density ratio (c) of (a, b).

Python package for Lagrangian filtering (Shakespeare et al., 2021) is used with the parameters set as follows: the particle-tracking window is ± 3 days; the time step for particle tracking is 25 s, which is exactly the time-marching step of the LLC4320 simulation; a fourth-order Butterworth filter, which is the default setting, is applied; the cutoff frequency is the inertial frequency at 10°N which is smaller than the minimum latitude (i.e., 15°N) of the study region and with this choice of the cutoff frequency we seek to extract IGWs as completely as possible. For Lagrangian filtering, wave variables are the outputs of the Python package and the difference between the

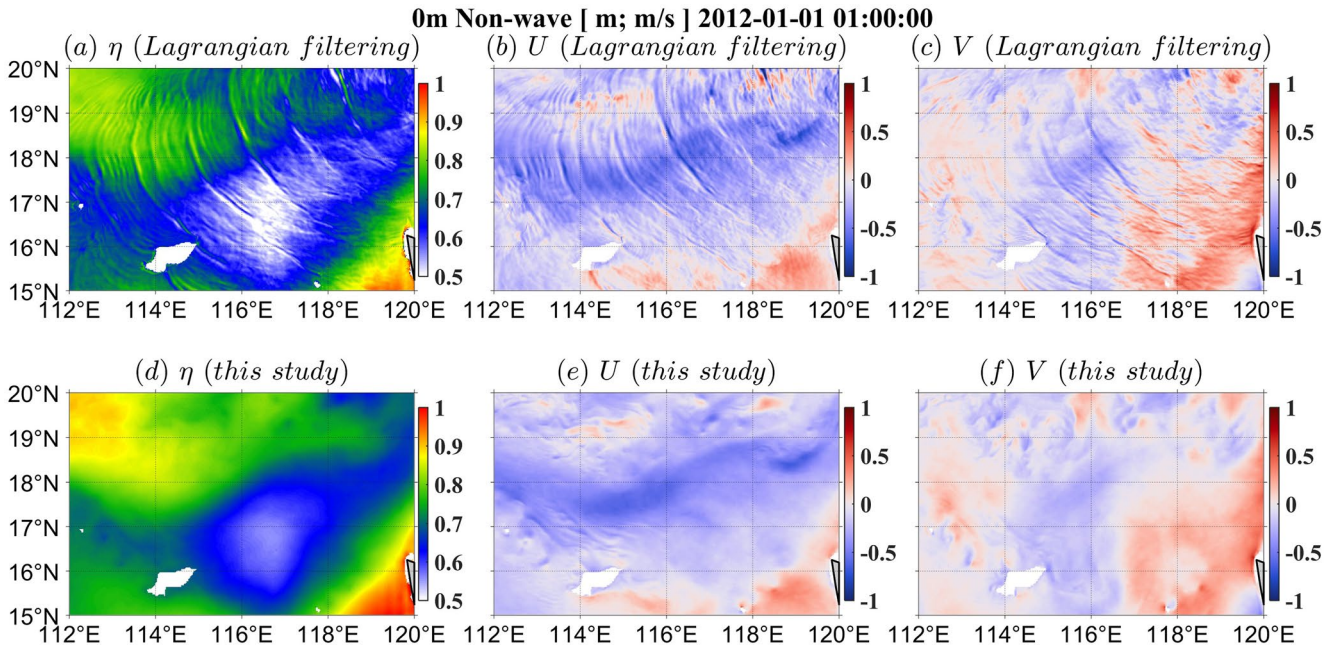

Figure 14. Non-wave (a, d) sea surface height, (b, e) zonal velocity, and (c, f) meridional velocity decomposed using (a–c) Lagrangian filtering and the (d–f) proposed decomposition methodology.

full-flow and wave variables gives non-wave variables. For our decomposition methodology, the decomposed barotropic tides, low-mode IGWs, and high-mode IGWs are summed to get wave variables; summing large-scale currents, mesoscale flows and submesoscale motions gives non-wave variables. Obviously, non-wave variables obtained from Lagrangian filtering contain obvious propagating internal tides (Figures 14a–14c), which are not identifiable in non-wave variables from our decomposition (Figures 14d–14f). Given that wave and non-wave variables sum to the full by definition, at least for the case considered here, Lagrangian filtering seems to recover less accurate waves (Figure 15).

Given the success revealed by previous studies (e.g., Bachman et al., 2020; Shakespeare et al., 2021) in using Lagrangian filtering, more careful and systematic comparisons between the proposed methodology and Lagrangian filtering should be conducted in the future. However, it should be obvious at this stage that the dynamics-based flow decomposition approach developed in this study is valid and useful.

5.4. Application of the Methodology to Other Regions

To examine its applicability to oceanic regions with different dynamical regimes, we perform the same decomposition for.

- three other regions in the SCS with distinctly differing tidal and mesoscale energy;
- one region in the North Pacific Subtropical Countercurrent area with high mesoscale energy and relatively low tidal energy;
- and one region in the Kuroshio Extension area with strong mesoscale activity and weak tides.

The key steps of the proposed methodology are to (a) extract low-mode IGWs and (b) separate high-mode IGWs from submesoscale flows. Since it is very difficult to unambiguously assess the isolated high-mode IGWs which are especially coupled with and modulated by submesoscale flows, we only show the extraction of low-mode IGWs in those regions. Figure 16 presents the correlation between the derived and directly decomposed velocities for low-mode IGWs over the entire simulation period. It is clear that extremely high correlation arises in all the regions, confirming the applicability and generality of the proposed methodology. Previous studies suggested that in the open ocean, the interior mesoscale flows can be faithfully reconstructed (Isern-Fontanet et al., 2006, 2008; LaCasce, 2012; LaCasce & Mahadevan, 2006; Lacasce & Wang, 2015; Lapeyre & Klein, 2006; Liu et al., 2019; Qiu et al., 2016; J. Wang et al., 2013); subsurface velocities of IGWs can be well estimated using vertical

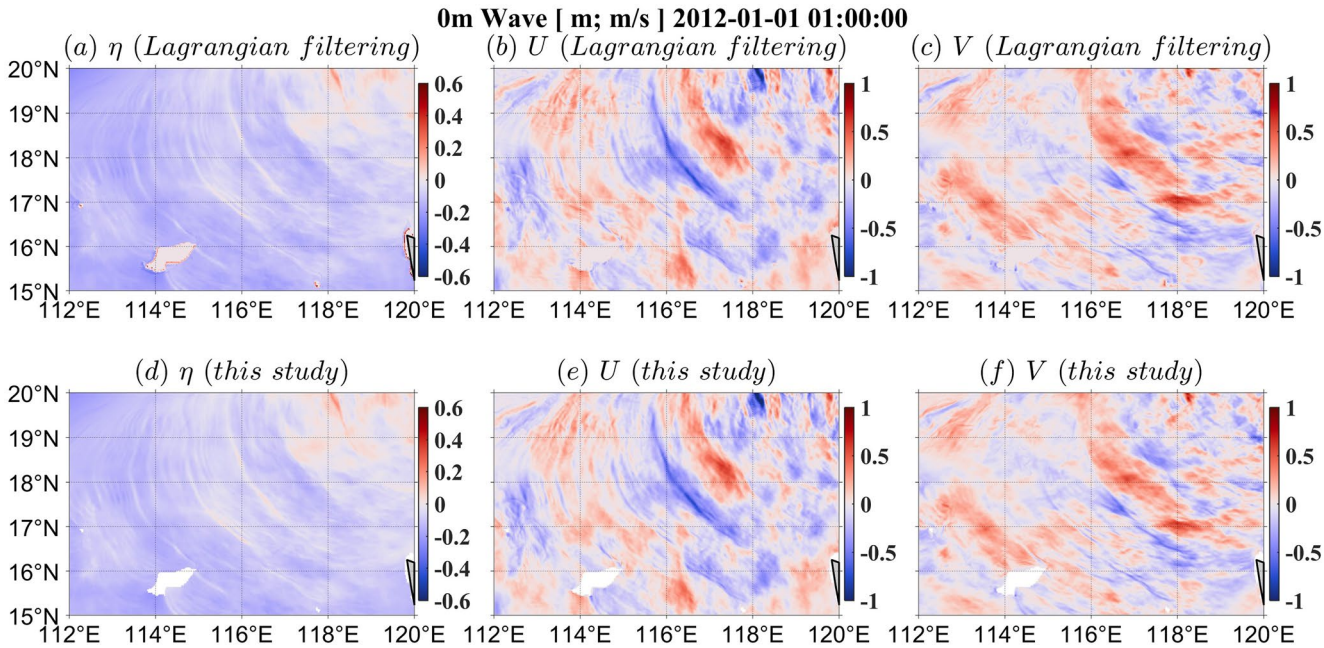

Figure 15. Wave (a, d) sea surface height, (b, e) zonal velocity, and (c, f) meridional velocity decomposed using (a–c) Lagrangian filtering and the (d–f) proposed decomposition methodology.

normal-mode structures (Ray & Cartwright, 2001; Zhao, 2017; Zhao et al., 2016). We actually find that the vertical reconstruction of IGWs is more straightforward and accurate than that of mesoscale motions because SSH of IGWs from different vertical modes can be directly separated from the first step of the decomposition (i.e., the IGWs-isolating step) without additional assumptions as introduced in interior mesoscale flow reconstruction. Therefore, it is anticipated that the dynamical flow decomposition based on SSH and the subsequent dynamical inference of interior flow structures can be applied to the world ocean. As such, 4D process-associated flow fields are recovered using solely SSH data.

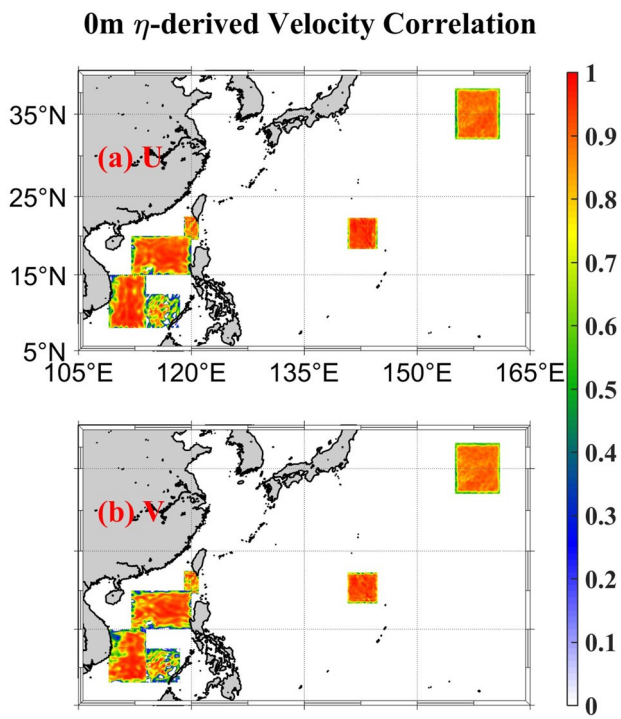

Figure 16. Pointwise correlations over the simulation period between the derived (from the decomposed sea surface height) and (a) directly decomposed zonal and (b) meridional velocity for low-mode internal gravity waves.

6. Summary

In this study, we have developed methodology for decomposing multiscale oceanic motions by virtue of their dynamical characteristics. The methodology is illustrated in the central basin of the SCS with numerically simulated flows from a tide-resolving and submesoscale-admitting MITgcm simulation. It is shown that the simulated large-scale currents, barotropic tides, low-mode IGWs, mesoscale flows, submesoscale flows, and high-mode IGWs can be isolated in a dynamically consistent manner and in a way seeming at least as good as Lagrangian filtering. In particular, the separation of submesoscale flows from high-mode IGWs effectively addresses the effect of aliasing and may apply to spontaneously generated IGWs which do not usually feel oceanic vertical boundaries and thus have complicated dispersion relations. This specific attempt may help reveal the compelling mystery of submesoscale-IGWs coupling (McWilliams, 2016). The proposed methodology also works well in other regions of the SCS and the open ocean, indicating the applicability of these methods in the global ocean. We expect that applications of the proposed decomposition methodology would further advance dynamical understanding of multiscale interactions of oceanic flows. For example, the energy transfers among different oceanic motions could be quantified quite straightforwardly from the decomposed flow components. These are objectives to be explored in ongoing and future studies.

We finally offer two caveats related to the proposed methodology. First of all, the proposed methodology relies on the homogeneity assumption inherent to the Fourier transform. The common trick to alleviate this issue is to partition the large study region into many small ($\sim 5° \times 5°$) boxes and perform the Fourier transform on one box each time (Qiu et al., 2018; Torres et al., 2018; Zaron, 2019; Zhao et al., 2019). This trick, more widely used in frequency spectral analysis of time-series data which are cut into several overlapping segments, can somewhat result in a balance between the assumption of homogeneity and the complexity of real flows. Moreover, Equation 9 would fail in the equatorial regions where the dynamical contrasts between submesoscale motions and high-mode IGWs require further explorations.

Data Availability Statement

The MATLAB code to perform the proposed decomposition is freely available at https://doi.org/10.5281/zenodo.7620637 (C. Wang et al., 2023). The ETOPO1 bathymetry data can be downloaded from https://doi.org/10.7289/V5C8276M (Amante & Eakins, 2009). The World Ocean Atlas (WOA2018) can be accessed from https://www.ncei.noaa.gov/archive/accession/NCEI-WOA18 (Boyer et al., 2018). The LLC4320 simulation output is available at https://data.nas.nasa.gov/ecco/data.php?dir=/eccodata/llc_4320 (Menemenlis, 2021).

Acknowledgments
This work was supported by the National Natural Science Foundation of China (91858201, 42076013, 92258301, 41721005, and 41890801) and the Natural Science Foundation of Fujian Province of China (2021J02005 and 2019J05009). We thank Robert Scott for sharing his code for the calculation of frequency-wavenumber spectra (http://stockage.univ-brest.fr/~scott/scripts.html). Angus Gibson and Callum Shakespeare from Australian National University are thanked for their helps in the installation of the Python package *Lagrangian filtering* (https://github.com/angus-g/lagrangian-filtering). The constructive feedbacks from the Editor (Stephen Griffies) and three anonymous reviewers greatly improved this paper. This work is a part of C. Wang's PhD research at the Dynamical Oceanography Group (DyOG) of Xiamen University, C. Wang would like to thank all other members of DyOG for their kind efforts to create an atmosphere which is scientifically stimulating and socially comfortable.

References

Amante, C., & Eakins, B. W. (2009). ETOPO1 1 arc-minute global relief model: Procedures, data sources and analysis. NOAA technical memorandum NESDIS NGDC-24 [Dataset]. National Geophysical Data Center, NOAA. https://doi.org/10.7289/V5C8276M

Arbic, B. K., Alford, M. H., Ansong, J. K., Buijsman, M. C., Ciotti, R. B., Farrar, J. T., et al. (2018). A Primer on global internal tide and internal gravity wave continuum modeling in HYCOM and MITgcm. In E. P. Chassignet, A. Pascual, J. Tintoré, & J. Verron (Eds.), *New frontiers in operational Oceanography* (pp. 307–392). GODAE OceanView. https://doi.org/10.17125/gov2018.ch13

Arbic, B. K., Müller, M., Richman, J. G., Shriver, J. F., Morten, A. J., Scott, R. B., et al. (2014). Geostrophic turbulence in the frequency–wavenumber domain: Eddy-driven low-Frequency variability. *Journal of Physical Oceanography*, *44*(8), 2050–2069. https://doi.org/10.1175/jpo-d-13-054.1

Bachman, S. D., Shakespeare, C. J., Kleypas, J., Castruccio, F. S., & Curchitser, E. (2020). Particle-based lagrangian filtering for locating wave-generated thermal refugia for coral reefs. *Journal of Geophysical Research: Ocean*, *125*(7), 1–24. https://doi.org/10.1029/2020JC016106

Barkan, R., Winters, K. B., & Mcwilliams, J. C. (2017). Stimulated imbalance and the enhancement of eddy kinetic energy dissipation by internal waves. *Journal of Physical Oceanography*, *47*(1), 181–198. https://doi.org/10.1175/JPO-D-16-0117.1

Bartello, P. (1995). Geostrophic adjustment and inverse cascades in rotating stratified turbulence. *Journal of the Atmospheric Sciences*, *52*(24), 4410–4428. https://doi.org/10.1175/1520-0469(1995)052<4410:GAAICI>2.0.CO;2

Boyer, T. P., Garcia, H. E., Locarnini, R. A., Zweng, M. M., Mishonov, A. V., Reagan, J. R., et al. (2018). World Ocean Atlas 2018 [Dataset]. NOAA National Centers for Environmental Information. Retrieved from https://www.ncei.noaa.gov/archive/accession/NCEI-WOA18

Bühler, O. (2009). *Waves and mean flows*. Cambridge University Press.

Bühler, O., Callies, J., & Ferrari, R. (2014). Wave–vortex decomposition of one-dimensional ship-track data. *Journal of Fluid Mechanics*, *756*, 1007–1026. https://doi.org/10.1017/jfm.2014.488

Capet, X., McWilliams, J. C., Molemaker, M. J., & Shchepetkin, A. F. (2008). Mesoscale to submesoscale transition in the California current system. Part I: Flow structure, eddy flux, and observational tests. *Journal of Physical Oceanography*, *38*(1), 29–43. https://doi.org/10.1175/2007JPO3671.1

Chen, G., Hou, Y., & Chu, X. (2011). Mesoscale eddies in the South China Sea: Mean properties, spatiotemporal variability, and impact on thermohaline structure. *Journal of Geophysical Research*, *116*(C6), 1–19. https://doi.org/10.1029/2010JC006716

Cheng, X., & Qi, Y. (2010). Variations of eddy kinetic energy in the South China Sea. *Journal of Oceanography*, *66*(1), 85–94. https://doi.org/10.1007/s10872-010-0007-y

Chu, X., Chen, G., & Qi, Y. (2020). Periodic mesoscale eddies in the South China Sea. *Journal of Geophysical Research: Ocean*, *125*, 1–15. https://doi.org/10.1029/2019JC015139

Danioux, E., Vanneste, J., Klein, P., & Sasaki, H. (2012). Spontaneous inertia-gravity-wave generation by surface-intensified turbulence. *Journal of Fluid Mechanics*, *699*, 153–173. https://doi.org/10.1017/jfm.2012.90

Dushaw, B. D. (2015). An empirical model for mode-1 internal tides derived from satellite altimetry: Computing accurate tidal predictions at arbitrary points over the world oceans (p. 114).

Ferrari, R., & Wunsch, C. (2009). Ocean circulation kinetic energy: Reservoirs, sources, and sinks. *Annual Review of Fluid Mechanics*, *41*(1), 253–282. https://doi.org/10.1146/annurev.fluid.40.111406.102139

Fu, L.-L., Keffer, T., Niiler, P., & Wunsch, C. (1982). Observations of mesoscale variability in the western North Atlantic: A comparative study. *Journal of Marine Research*, *40*, 809–848.

Garcia, D. (2010). Robust smoothing of gridded data in one and higher dimensions with missing values. *Computational Statistics & Data Analysis*, *54*(4), 1167–1178. https://doi.org/10.1016/j.csda.2009.09.020

Gill, A. (1982). *Atmosphere-ocean dynamics* (p. 662). Academic Press.

Hu, J., Kawamura, H., Hong, H., & Qi, Y. (2000). A review on the currents in the South China Sea: Seasonal circulation, South China Sea warm current and Kuroshio intrusion. *Journal of Oceanography*, *56*, 607–624.

Isern-Fontanet, J., Chapron, B., Lapeyre, G., & Klein, P. (2006). Potential use of microwave sea surface temperatures for the estimation of ocean currents. *Geophysical Research Letters*, *33*(24), 1–5. https://doi.org/10.1029/2006GL027801

Isern-Fontanet, J., Lapeyre, G., Klein, P., Chapron, B., & Hecht, M. W. (2008). Three-dimensional reconstruction of oceanic mesoscale currents from surface information. *Journal of Geophysical Research*, *113*(C9), 1–17. https://doi.org/10.1029/2007JC004692

Jones, C. S., Xiao, Q., Abernathey, R. P., & Smith, K. S. (2023). Using Lagrangian filtering to remove waves from the ocean surface velocity field. [Preprint]. EarthArXiv. https://doi.org/10.31223/X5D352

Kunze, E. (1985). Near-inertial wave propagation in geostrophic shear. *Journal of Physical Oceanography*, *15*(5), 544–565. https://doi.org/10.1175/1520-0485(1985)015<0544:NIWPIG>2.0.CO;2

LaCasce, J. (2012). Surface quasigeostrophic solutions and baroclinic modes with exponential stratification. *Journal of Physical Oceanography*, *42*(4), 569–580. https://doi.org/10.1175/JPO-D-11-0111.1

LaCasce, J., & Mahadevan, A. (2006). Estimating subsurface horizontal and vertical velocities from sea-surface temperature. *Journal of Marine Research*, *64*(5), 695–721. https://doi.org/10.1357/002224006779367267

Lacasce, J. H., & Wang, J. (2015). Estimating subsurface velocities from surface fields with idealized stratification. *Journal of Physical Oceanography*, *45*(9), 2424–2435. https://doi.org/10.1175/JPO-D-14-0206.1

Lapeyre, G., & Klein, P. (2006). Dynamics of the upper oceanic layers in terms of surface quasigeostrophy theory. *Journal of Physical Oceanography*, *36*(2), 165–176. https://doi.org/10.1175/JPO2840.1

Leith, C. E. (1980). Nonlinear normal mode initialization and quasi-geostrophic theory. *Journal of the Atmospheric Sciences*, *37*(5), 958–968. https://doi.org/10.1175/1520-0469(1980)037<0958:NNMIAQ>2.0.CO;2

Liang, X. S. (2016). Canonical transfer and multiscale energetics for primitive and quasigeostrophic atmospheres. *Journal of the Atmospheric Sciences*, *73*(11), 4439–4468. https://doi.org/10.1175/JAS-D-16-0131.1

Lien, R.-C., & Müller, P. (1992). Normal-mode decomposition of small-scale oceanic motions. *Journal of Physical Oceanography*, *22*(12), 1583–1595. https://doi.org/10.1175/1520-0485(1992)022<1583:NMDOSS>2.0.CO;2

Lin, H., Liu, Z., Hu, J., Menemenlis, D., & Huang, Y. (2020). Characterizing meso- to submesoscale features in the South China Sea. *Progress in Oceanography*, *188*, 102420. https://doi.org/10.1016/j.pocean.2020.102420

Liu, L., Xue, H., & Sasaki, H. (2019). Reconstructing the ocean interior from high-resolution sea surface information. *Journal of Physical Oceanography*, *49*(12), 3245–3262. https://doi.org/10.1175/JPO-D-19-0118.1

Luecke, C. A., Arbic, B. K., Richman, J. G., Shriver, J. F., Alford, M. H., Ansong, J. K., et al. (2020). Statistical comparisons of temperature variance and kinetic energy in global ocean models and observations: Results from mesoscale to internal wave frequencies. *Journal of Geophysical Research: Ocean*, *125*(5), e2019JC015306. https://doi.org/10.1029/2019JC015306

Majda, A. (2003). *Introduction to PDEs and waves for the atmosphere and ocean* (Vol. 9). American Mathematical Soc.

Marshall, J., Adcroft, A., Hill, C., Perelman, L., & Heisey, C. (1997). A finite-volume, incompressible Navier-Stokes model for studies of the ocean on parallel computers. *Journal of Geophysical Research*, *102*(C3), 5753–5766. https://doi.org/10.1029/96JC02775

McWilliams, J. C. (2016). Submesoscale currents in the ocean. *Proceedings of the Royal Society A: Mathematical, Physical and Engineering Sciences*, *472*(2189), 20160117. https://doi.org/10.1098/rspa.2016.0117

Menemenlis, D. (2021). llc4320 [Dataset]. ECCO Data Portal. Retrieved from https://data.nas.nasa.gov/ecco/data.php?dir=/eccodata/llc_4320

Müller, M., Arbic, B. K., Richman, J. G., Shriver, J. F., Kunze, E. L., Scott, R. B., et al. (2015). Toward an internal gravity wave spectrum in global ocean models. *Geophysical Research Letters*, *42*(9), 3474–3481. https://doi.org/10.1002/2015GL063365

Müller, P. (1984). Small-scale vortical motions. In *Internal gravity waves and small-scale turbulence: Proc. "Aha Huliko"a Hawaiian winter workshop*. (pp. 249–262). University of Hawai'i at Mānoa.

Müller, P. (1988). *Vortical motions* (Vol. 46, pp. 285–301). Elsevier Oceanography Series.

Nagai, T., Tandon, A., Kunze, E., & Mahadevan, A. (2015). Spontaneous generation of near-inertial waves by the Kuroshio Front. *Journal of Physical Oceanography*, *45*(9), 2381–2406. https://doi.org/10.1175/JPO-D-14-0086.1

Ni, Q., Zhai, X., Wilson, C., Chen, C., & Chen, D. (2021). Submesoscale eddies in the South China Sea. *Geophysical Research Letters*, *48*(6), e2020GL091555. https://doi.org/10.1029/2020GL091555

Pawlowicz, R., Beardsley, B., & Lentz, S. (2002). Classical tidal harmonic analysis including error estimates in MATLAB using T_TIDE. *Computers & Geosciences*, *28*(8), 929–937. https://doi.org/10.1016/S0098-3004(02)00013-4

Pedlosky, J. (2003). *Waves in the ocean and atmosphere* (p. 260). Springer Berlin Heidelberg.

Ponte, A. L., Klein, P., Dunphy, M., & Le Gentil, S. (2017). Low-mode internal tides and balanced dynamics disentanglement in altimetric observations: Synergy with surface density observations. *Journal of Geophysical Research: Ocean*, *122*(3), 2143–2155. https://doi.org/10.1002/2016JC012214

Ponte, R., Chaudhuri, A., & Vinogradov, S. (2015). Long-period tides in an atmospherically driven, stratified ocean. *Journal of Physical Oceanography*, *45*(7), 1917–1928. https://doi.org/10.1175/JPO-D-15-0006.1

Qiu, B., Chen, S., Klein, P., Torres, H., Wang, J., Fu, L. L., & Menemenlis, D. (2019). Reconstructing upper ocean vertical velocity field from sea surface height in the presence of unbalanced motion. *Journal of Physical Oceanography*, *49*(1), 55–79. https://doi.org/10.1175/JPO-D-19-0172.1

Qiu, B., Chen, S., Klein, P., Ubelmann, C., Fu, L. L., & Sasaki, H. (2016). Reconstructability of three-dimensional upper-ocean circulation from SWOT sea surface height measurements. *Journal of Physical Oceanography*, *46*(3), 947–963. https://doi.org/10.1175/JPO-D-15-0188.1

Qiu, B., Chen, S., Klein, P., Wang, J., Torres, H., Fu, L.-L., & Menemenlis, D. (2018). Seasonality in transition scale from balanced to unbalanced motions in the world ocean. *Journal of Physical Oceanography*, *48*(3), 591–605. https://doi.org/10.1175/JPO-D-17-0169.1

Ray, R. D., & Cartwright, D. E. (2001). Estimates of internal tide energy fluxes from Topex/Poseidon altimetry: Central North Pacific. *Geophysical Research Letters*, *28*(7), 1259–1262. https://doi.org/10.1029/2000GL012447

Rocha, C. B., Chereskin, T. K., Gille, S. T., & Menemenlis, D. (2016). Mesoscale to submesoscale wavenumber spectra in Drake Passage. *Journal of Physical Oceanography*, *46*(2), 601–620. https://doi.org/10.1175/jpo-d-15-0087.1

Rocha, C. B., Gille, S. T., Chereskin, T. K., & Menemenlis, D. (2016). Seasonality of submesoscale dynamics in the Kuroshio extension. *Geophysical Research Letters*, *43*(21), 11304–11311. https://doi.org/10.1002/2016GL071349

Savage, A. C., Arbic, B. K., Alford, M. H., Ansong, J. K., Farrar, J. T., Menemenlis, D., et al. (2017). Spectral decomposition of internal gravity wave sea surface height in global models. *Journal of Geophysical Research: Ocean*, *122*(10), 7803–7821. https://doi.org/10.1002/2017JC013009

Savage, A. C., Arbic, B. K., Richman, J. G., Shriver, J. F., Alford, M. H., Buijsman, M. C., et al. (2017). Frequency content of sea surface height variability from internal gravity waves to mesoscale eddies. *Journal of Geophysical Research: Ocean*, *122*(3), 2519–2538. https://doi.org/10.1002/2016JC012331

Shakespeare, C. J., Gibson, A. H., Hogg, A. M. C., Bachman, S. D., Keating, S. R., & Velzeboer, N. (2021). A new open source implementation of Lagrangian filtering: A method to identify internal waves in high-resolution simulations. *Journal of Advances in Modeling Earth Systems*, *13*(10), e2021MS002616. https://doi.org/10.1029/2021MS002616

Shakespeare, C. J., & Hogg, A. M. C. (2017). Spontaneous surface generation and interior amplification of internal waves in a regional-scale ocean model. *Journal of Physical Oceanography*, *47*(4), 811–826. https://doi.org/10.1175/JPO-D-16-0188.1

Shakespeare, C. J., & Hogg, A. M. C. (2019). On the momentum flux of internal tides. *Journal of Physical Oceanography*, *49*(4), 993–1013. https://doi.org/10.1175/JPO-D-18-0165.1

Sugimoto, N., & Plougonven, R. (2016). Generation and backreaction of spontaneously emitted inertia-gravity waves. *Geophysical Research Letters*, *43*(7), 3519–3525. https://doi.org/10.1002/2016GL068219

Torres, H. S., Klein, P., Menemenlis, D., Qiu, B., Su, Z., Wang, J., et al. (2018). Partitioning ocean motions into balanced motions and internal gravity waves: A modeling study in anticipation of future space missions. *Journal of Geophysical Research: Ocean*, *123*(11), 8084–8105. https://doi.org/10.1029/2018JC014438

Torres, H. S., Klein, P., Siegelman, L., Qiu, B., Chen, S., Ubelmann, C., et al. (2019). Diagnosing ocean-wave-turbulence interactions from space. *Geophysical Research Letters*, *46*(15), 8933–8942. https://doi.org/10.1029/2019GL083675

von Storch, J.-S., Badin, G., & Oliver, M. (2019). The interior energy pathway: Inertia-gravity wave emission by oceanic flows. In C. Eden & A. Iske (Eds.), *Energy transfers in atmosphere and ocean. Mathematics of planet Earth* (Vol. 1). Springer. https://doi.org/10.1007/978-3-030-05704-6_2

Wang, C., Liu, Z., & Lin, H. (2022). Interpreting consequences of inadequate sampling of oceanic motions. *Limnology and Oceanography Letters*, *7*(5), 385–391. https://doi.org/10.1002/lol2.10260

Wang, C., Liu, Z., & Lin, H. (2023). On dynamical decomposition of multiscale oceanic motions (Version 2) [Software]. Zenodo. https://doi.org/10.5281/zenodo.7620637

Wang, G., Garcia, D., Liu, Y., de Jeu, R., & Johannes Dolman, A. (2012). A three-dimensional gap filling method for large geophysical datasets: Application to global satellite soil moisture observations. *Environmental Modelling & Software*, *30*, 139–142. https://doi.org/10.1016/j.envsoft.2011.10.015

Wang, J., Flierl, G. R., LaCasce, J. H., McClean, J. L., & Mahadevan, A. (2013). Reconstructing the ocean's interior from surface data. *Journal of Physical Oceanography*, *43*(8), 1611–1626. https://doi.org/10.1175/JPO-D-12-0204.1

Wang, J., Fu, L. L., Qiu, B., Menemenlis, D., Thomas Farrar, J., Chao, Y., et al. (2018). An observing system simulation experiment for the calibration and validation of the surface water ocean topography sea surface height measurement using in situ platforms. *Journal of Atmospheric and Oceanic Technology*, *35*(2), 281–297. https://doi.org/10.1175/JTECH-D-17-0076.1

Yan, T., Qi, Y., Jing, Z., & Cai, S. (2020). Seasonal and spatial features of barotropic and baroclinic tides in the northwestern South China Sea. *Journal of Geophysical Research: Ocean*, *125*(1), e2018JC014860. https://doi.org/10.1029/2018JC014860

Yu, X., Ponte, A. L., Elipot, S., Menemenlis, D., Zaron, E. D., & Abernathey, R. (2019). Surface kinetic energy distributions in the global oceans from a high-resolution numerical model and surface drifter observations. *Geophysical Research Letters*, *46*(16), 9757–9766. https://doi.org/10.1029/2019GL083074

Zaron, E. D. (2019). Baroclinic tidal sea level from exact-repeat mission altimetry. *Journal of Physical Oceanography*, *49*(1), 193–210. https://doi.org/10.1175/JPO-D-18-0127.1

Zhao, Z. (2014). Internal tide radiation from the Luzon strait. *Journal of Geophysical Research: Ocean*, *119*(8), 5434–5448. https://doi.org/10.1002/2014jc010014

Zhao, Z. (2017). The global mode-1 S_2 internal tide. *Journal of Geophysical Research: Ocean*, *122*(11), 8794–8812. https://doi.org/10.1002/2017JC013112

Zhao, Z., Alford, M. H., Girton, J. B., Rainville, L., & Simmons, H. L. (2016). Global observations of open-ocean mode-1 M_2 internal tides. *Journal of Physical Oceanography*, *46*(6), 1657–1684. https://doi.org/10.1175/JPO-D-15-0105.1

Zhao, Z., Wang, J., Menemenlis, D., Fu, L.-L., Chen, S., & Qiu, B. (2019). Decomposition of the multimodal multidirectional M_2 internal tide field. *Journal of Atmospheric and Oceanic Technology*, *36*(6), 1157–1173. https://doi.org/10.1175/JTECH-D-19-0022.1

Zu, T., Gan, J., & Erofeeva, S. Y. (2008). Numerical study of the tide and tidal dynamics in the South China Sea. *Deep Sea Research Part I: Oceanographic Research Papers*, *55*(2), 137–154. https://doi.org/10.1016/j.dsr.2007.10.007